Final Report- External Grant Award No. G09AP00017

EFFECTS OF STYLE OF FAULTING ON EARTHQUAKE GROUND MOTIONS IN NMSZ

Stephen Horton
Center for Earthquake Research and Information, University of Memphis
3890 Central Avenue
Memphis, TN 38152
Telephone: (901) 678-4896
FAX: (901) 678-4734
Email: shorton@memphis.edu

Start Date: January 1, 2009
End Date: March 31, 2011

ABSTRACT

This study investigates the effects of style of faulting on earthquake ground motion in the New Madrid seismic zone (NMSZ). I undertake a detailed analysis of local waveform data using a multistage processing method to produce empirical attenuation relations for frequencies between 1 and 16 Hz. The dataset consists of 854 local events of magnitude $1.6 \leq M \leq 4.3$ recorded at hypocentral-distances ranging from 5.6 to 145 km. The modelling procedure yields a r^{-1} geometrical spreading with $Q(f) = 660 f^{0.35}$ within the first 60 km hypocentral distance. Beyond 60 km distance, the geometrical spreading changes to $r^{0.5}$. Reverse fault events tend to have higher ground motion near the source than for strike-slip fault events for frequencies greater than 8 Hz. At lower frequencies, no difference is discerned for the two styles of faulting. An average kappa value of 0.011± 0.004 is estimated for the region. Events of $M_W \geq 3.5$ have an average stress drop of 138 bar.

TABLE OF CONTENTS

1 Introduction 1
1.1 NMSZ tectonic setting and seismicity 2
1.2 Geological setting 5

2 Method 6
2.1 Coda waves 6
2.2 Coda normalization application 7
2.3 Peak motion regression 8
2.3.1 Geometrical spreading and Q 8
2.3.2 Source excitation 9
2.3.3 Site effect 9

3 Data processing and modelling 9
3.1 Data set 9
3.2 Duration 10
3.3 The distance term D 12
3.3.1 Initial estimate of D 12
3.3.2 Forward modelling 13
3.3.3 Average attenuation 14
3.3.4 Attenuation for different styles-of-fault 17
3.4 Excitation 20
3.4.1 Duration magnitude and Moment magnitude 24
3.4.2 Stress drop 25

4 Conclusion 28
4.1 Future studies 28
References Cited 29
Appendices 36
A Supplementary figures for estimating the distance term D 36
B Regression of coda-normalized peak velocities 48
C Dataset used to estimate seismic moment 49

1 Introduction

Ground motion prediction as a function of earthquake magnitude and distance is an important tool in the analysis of seismic hazard. These relations are typically developed empirically by a regression of recorded ground motion amplitude data versus magnitude, distance, and possibly other predictive variables. In the Central and Eastern US stochastic based ground-motion simulations are computed for a variety of magnitudes and distances. Peak ground motions measured from these simulations are the data regressed to obtain these relations.

The effects of style-of-faulting on ground motion in the New Madrid seismic zone (NMSZ) is one of the variables which has not been considered in previous ground-motion relations for eastern North America (e.g. Atkinson, 1984; Boore and Atkinson, 1987; Toro and McGuire, 1987; EPRI, 1988; Atkinson and Boore, 1990, 1995; Samiezade-Yard *et al.*, 1996; Atkinson and Boore, 2006). However, different styles-of-faulting have produced systematically different ground motion in recent western U.S. ground motion models distinguishing between reverse and strike-slip.

Idriss was the first to include a factor for style of faulting. He (1985; 1987; 1991), derived discrete equations for peak acceleration as a function of spectral ordinates. His relationships include a factor of one for reverse fault and zero for strike slip fault as a style-of-faulting factor, although the factors are independent of other variables.

In a summary of previous studies on estimating horizontal response spectra and peak acceleration for shallow earthquakes in western North America, Boore *et al.* (1997) estimated the style-of-faulting factor independently for each period between 0.1 to 2.0 seconds. They had a relationship that factored reverse faults as having larger constant than strike slip faults. Their results showed the difference in style-of-faulting factor maintained a constant margin as it varied slightly with period (frequency).

Campbell and Bozorgnia (2003) examined the distance and magnitude dependence of style-of-faulting factor for peak acceleration. They found that both the horizontal and vertical spectra had the same tendency toward higher amplitudes for reverse and thrust faulting at short-to-mid periods compared to strike slip faulting. These differences become negligible at periods greater than about 2 sec. They found differences in median-predicted spectral acceleration among strike-slip, reverse, and thrust-faulting earthquakes to be consistent with differences in dynamic stress drop.

Later Campbell and Bozorgnia (2006; 2008) defined the style-of-faulting factor as a term that introduces a new parameter, depth, to the top of coseismic rupture. The new parameter indicates whether or not coseismic rupture extends to the surface. This was most significant at short periods for reverse faulting, with ground motion being significantly higher especially for reverse faulting when rupture did not break to the surface. The reverse-fault events create ground motions approximately 28% higher than those from crustal strike-slip events.

The NMSZ is the most seismically active area of the central and eastern North America. During the winter of 1811 and 1812, three catastrophic earthquakes occurred in the region (Nuttli, 1973; Mitchell *et al.*, 1991; Johnston, 1996; Johnston and Schweig, 1996). The three earthquakes were felt throughout much of the U.S. and as far away as Quebec (Nuttli, 1973). Paleoliquefaction studies show that very large earthquakes

occurred in A.D. 900 ± 100 and A.D. 1450 ± 150 years, suggesting a pattern of repeating earthquakes with a return period around 500 years (Tuttle *et al.*, 2002). The possibility of recurrence of such large earthquakes and the greatly increased population of the area provides an impetus for ground motion estimation and seismic hazard analysis. Currently, NMSZ has 200 earthquakes recorded per year by the Cooperative New Madrid Seismic Network (CNMSN). Since the year 2000, the CNMSN has recorded regional events of magnitude ranging from 0.3 to 4.1.

This study primarily evaluates the effects of style of faulting on ground motions. I determine the average attenuation, site, and source properties for the region for all types of earthquakes combined together, then separately for strike-slip and reverse-slip earthquakes in the NMSZ. The site properties should not vary with earthquake type. The attenuation term includes a frequency-dependent attenuation operator, $Q(f)$, and a geometric spreading function. An important factor also to be determined is the scaling of signal duration with distance. Earthquake damage is strongly related to ground motion duration. Short duration motions with high acceleration may not produce enough load reversal to damage buildings but those with long duration may (Kramer, 1996). Signal duration is also important factor required to estimate the peak-motions using stochastic models in the theory described by Boore (1983). These terms are the primary inputs to stochastic ground motion simulation techniques such as SMSIM (Boore, 2002) and FINSIM (Beresnev and Atkinson, 1998).

The other important task is to estimate stress drop variation with seismic moment, so as to provide important constraints for source scaling based on earthquake type. All these products put together will contribute to deriving a realistic ground motion model for the NMSZ. This will be achieved by detailed analysis of local waveform data using a multistage processing method (e.g. Raoof *et al.*, 1999; and Malagnini *et al.*, 2000) to produce empirical attenuation relations for frequencies between 1 and 16 Hz.

1.1 NMSZ tectonic setting and seismicity

The NMSZ is spatially associated with the Reelfoot rift. The northeast-trending Reelfoot rift is a geologic feature formed during a plate wide extensional event in the early Cambrian (Burke and Dewey, 1973) in response to the breakup of the supercontinent Rhodinia (Thomas 1985; 1991; 2006) extending north into the Illinois Basin (McBride *et al.*, 2003). The rift was later reactivated during the Cretaceous, in response to closing of the Iapatus Ocean, to form the Mississippi embayment (Ervin and McGinnis, 1975). The Reelfoot Rift was elevated during this period and the Pascola arch formed separating the Reelfoot Rift from the Illinois Basin to the north. This reactivation was accompanied by intrusive activity as inferred from bands of magnetic and gravity lows and highs (Cox and VanArsdale, 1997; 2002). The rift is bounded by two parallel, 300 km long, normal displacement faults trending NE-SW, separated by a width of about 70 km. The Precambrian surface is displaced as much as 3 km on the northwestern bounding fault with nearly vertical dip to the southeast (Parrish and VanArsdale, 2004). Approximately 3 km of displacement is observable on the southeastern bounding fault with nearly vertical dip to the northwest.

A compressive stress field has existed since the Cretaceous with the compression axis oriented ENE to EW. This Cretaceous stress regime of the midcontinent (Zoback and Zoback, 1980) has apparently reactivated northeast striking rift-axis and rift-margin faults

as right lateral strike-slip faults and northwest striking, southwest dipping faults as reverse or thrust faults (Chiu *et al.*, 1992). The NMSZ fault system can be divided into 4 different groups based on visible seismic trends. These groups consist of a Southern Arm, Central Arm, Northern Arm, and Northwestern Arm. Figure 1, adopted from Johnson (2008), shows some focal mechanism solutions and their locations. The coloured dots are events used in Johnson's (2008) study while the gray dots in the background are locations of some seismicity from 1974 to 2007 as published by Johnson (2008).

A focal mechanism study by Johnson (2008) produced 290 focal mechanism solutions for events recorded between the year 2000 and 2007. About 44% of these events had strike-slip nodal planes, while 37% of the events were thrust earthquakes and the rest were normal faults. The major strike-slip nodal planes, that match the seismicity, are oriented at ~50° and ~30° parallel to the Southern Arm and the Northern Arm respectively (Figure 1). The reverse faults trends are more prominent in the Central Segment oriented at about 147° and 0°. Normal faults in the NMSZ show a variety of nodal plane orientations. Cross sections of the Central Segment reveal that the only concentration of normal events in the hanging wall occurs slightly in the Mid-Central Segment. Although all the three groups of focal mechanisms appear in all the rift segments, the Central Segment focal types have more complex spatial patterns.

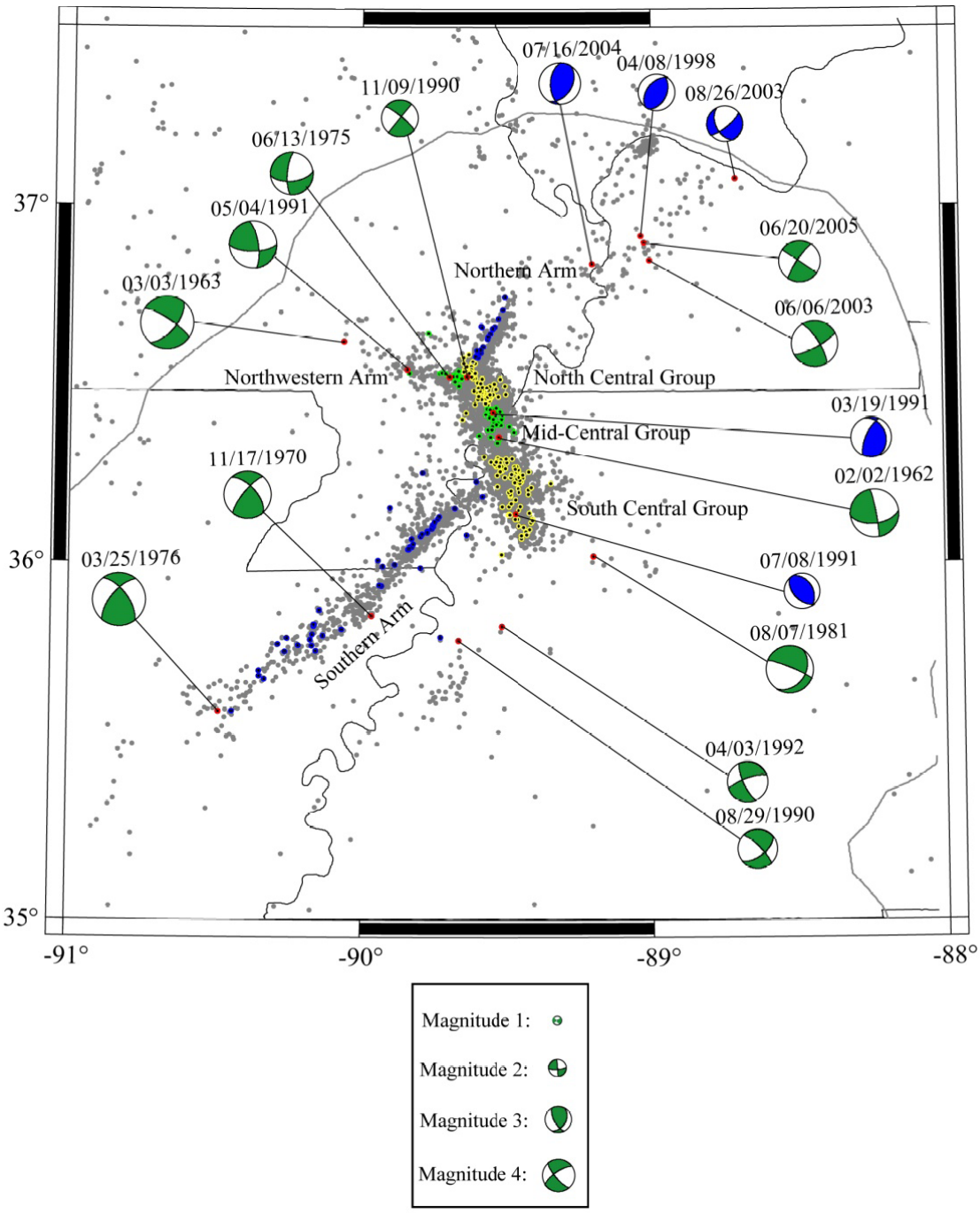

Figure 1-1: Figure extracted from Johnson (2008) showing focal mechanisms from past studies in NMSZ. Green focal mechanisms are strike-slip earthquakes, and blue focal mechanisms are reverse earthquakes. Locations of earthquake focal mechanisms from Johnson (2008) study are shown in different colours in order to illustrate how each focal mechanism set is grouped. Gray dots in the background are locations of some seismicity from 1974 to 2007. The thick gray line is an outline of the Mississippi Embayment.

1.2 Geological setting

The Mississippi Embayment, hosting NMSZ, is a southwest-plunging sedimentary trough filled with Upper Cretaceous (post mid- Cenomanian) to upper Eocene (Priabonian) marine and deltaic sediments locally overlain by Pliocene (Piacenzian) and Quaternary fluvial deposits of the Mississippi River and its tributaries (Stearns, 1957; Murray, 1961; Cushing *et al.*, 1964; Autin *et al.*, 1991; Hosman and Weiss, 1991). The synclinal orientation roughly coincides with the present course of the Mississippi River. The embayment originated in the Late Cretaceous, with continued subsidence through the Eocene terminating by the earliest Oligocene. The Late Cretaceous to Recent clastic sediments average about 600m thickness in the study area, overlie Paleozoic cratonic shelf facies ranging from Cambrian to Pennsylvanian in age, thickening to about 1000m near Memphis, and feathering erosionally to zero thickness at the embayment margins (Dart, 1992). The Paleozoic section and underlying Proterozoic granitic basement are cut by northeast-striking faults, and this fault system defines the geographic extent of the Mississippi Embayment (Hildenbrand *et al.* 1982).

The general stratagraphic section for the seismogenic portion of the Reelfoot rift consists of Early Cambrian basal arkosic sandstone followed by the Early through Middle Cambrian Potsdam Supergroup consisting of sandstones, limestones and shales (Thomas, 1985; Howe and Thompson, 1984). Deposition kept pace with regional subsidence during Late Cambrian–Middle Ordovician time, resulting in the thick, shallow marine Knox carbonate Supergroup that overlies the rift (Thomas, 1985; Howe and Thompson, 1984). Middle Ordovician to Middle-Cretaceous rocks are largely missing above the rift, partly due to nondeposition (Permian–Late Cretaceous) and partly due to Late Paleozoic and/or Middle-Cretaceous uplift and erosion, which produced a major unconformity at the top of the Paleozoic section. This stratigraphy is fairly uniform within the embayment and allows us to use a common velocity model of the embayment. A good velocity model is useful in defining the source parameters of a given Earthquake.

2 Method

Ground motions from earthquakes depend on the mechanical properties of the earth materials and the heterogeneities found along their path, as well as, the strength of the earthquake source. A general form for a predictive ground motion relationship is modelled, as a logarithm of the peak values of narrow bandpass-filtered versions of the instrument corrected time histories (ground velocity in m/sec) at each frequency (Raoof *et al.*, 1999; and Malagnini *et al.*, 2000), as

$$\log a_s(f,r) = EXC(f) + D(r,f) + SITE(f) \tag{1}$$

where f represents frequency and r hypocentral distance, $a_s(f,r)$ is the peak amplitude of the ground motion carried by direct *S* waves, recorded at the hypocentral distance r. The term $EXC(f)$ represents (in terms of peak motion) the seismic source. $D(r,f)$ scales the ground motion with distance irrespective of magnitude and combines geometrical spreading, scattering and intrinsic absorption, $Q(f)$. $SITE(f)$ indicates the contributions of the site characteristics to the observed peak motion.

The relationship (1) has three unknown terms on the right hand side to be inverted. I solve this in two stages. To begin I derive a starting model for the path term, $D(r,f)$ that will be described as a piece-wise continuous function. This is done through coda normalization (Aki, 1980; Frankel *et al.*, 1990) that removes the effects of source and site from the logarithm of peak ground motion. The applicable constraints for using this normalization when considering coda properties are described in the next section. The normalized amplitudes, plotted as a function of distance, provide a magnitude-independent estimate of the decrease of amplitude with distance. This empirical estimate value of $D(r,f)$ is then fitted using a multi-linear geometrical spreading and the crustal parameter. Having solved for $D(r,f)$, I then perform an iterative, damped least-squares regression to estimate source excitation, and site.

2.1 Coda waves

The coda normalization technique was applied to remove the effects of instrument response, unknown source, and site effects and to isolate the attenuation in the mid- and lower-crust (Aki, 1980; Frankel *et al.*, 1990). Coda waves are defined as the continuous wave-trains in the tail portion of seismogram. Aki (1969) noticed that early portions of seismograms are composed of waves that propagate from the source and decrease with amplitude with increasing propagation distance, while the coda had similar amplitudes and spectral content at all stations independent of epicentral-distance.

The coda waves are created by the incoherent scattering from the random heterogeneity in the Earth's lithosphere. Aki and Chouet (1975) found that at around 1 Hz the coda is made of backscattering surface waves from heterogeneities in the shallow, low-Q lithosphere. They however observed a high Q for the coda at frequencies higher than 10 Hz, and deduced that the high Q eliminated the possibility that these waves are backscattering surface waves. They conclude that at these high frequencies the coda must be made of backscattering body waves from heterogeneities in the deep lithosphere. This technique is based upon the single-station method proposed by Aki (1980) who applied

this method to several earthquakes observed at different distances from a single station. For this study, this method is extended to use several stations.

The coda normalization technique is best applied at epicentral distances less than 100 km and at times greater than two times the S-wave travel time. At this distance and time, the spectrum of coda waves is the same at all nearby recording stations for an earthquake (Tsumura, 1967), and the power spectra of coda waves decays in the same manner at a station for all events within a given region (Rautian and Khalturin, 1978). The coda decay shape is independent of earthquake size for magnitudes less than 6, and coda amplitude differs with local geology at a recording site. These are commonly accepted characteristics of the coda that make it useful for this study.

2.2 Coda normalization application

A coda normalization technique (Aki, 1980; Frankel *et al.*, 1990) is used to obtain a starting model for $D(r, r_{\mathrm{ref}}, f)$ for the regressions on the peak amplitudes. By definition, the time-domain rms amplitudes of the narrow bandpass-filtered time histories are centered in windows over lapse time τ running along the seismic coda (i.e., $\tau \geq 2t_s$). This can be represented as,

$$\log\left[a_C\left(f,\tau,r\right)\right] = EXC_{Coda}(f) + C(f,\tau,r) + SITE_{Coda}(f) \tag{2}$$

By using the coda normalization method, a normalized function $C_{\mathrm{Norm}}(f,\tau)$ is empirically determined. $C(\tau,r,f)$ is the coda envelope shape that describes the decay of the coda spectral amplitude with lapsed time on the seismogram. The relative values of $C(\tau,r,f)$ for each frequency at the same time τ show the effect of scattering and anelastic attenuation of the coda spectrum. Equation (2) is of the same form as equation (1), and for that case we can compute the ratio,

$$a_{reduced}(r,f) = a_S(r,f)/a_C(f,\tau_{2S},r) \tag{3}$$

where $a_S(r,f)$ can be the peak amplitude of the direct *S* waves and a_C is the amplitude of coda at more than twice the S-wave arrival time (i.e. >2S). The essence of this method is that the ratio mathematically eliminates the source and site terms, assuming these terms are equivalent both for the S wave and the coda, and that coda generation is a linear process. This leads to

$$\log\left[a_{reduced}(r,f)\right] = D(r,f) - C(f,\tau_{2S},r) \tag{4}$$

By forcing $D\left(r,r_{ref},f\right) = 0$ at a reference distance, we fix the amplitude offset caused by $C(\tau,r,f)$. This constraint removes the contribution of $C(\tau,r,f)$ from equation (4), and the resultant is the $D\left(r,r_{ref},f\right)$ term normalized to zero at a reference distance. The

reference distance is arbitrary and is chosen only for the purpose of arithmetic. I then find $D(r, r_{ref}, f)$ by curve fitting and solve the term as a forward problem (as detailed below).

2.3 Peak motion regression

After defining the distance term, a regression of the peak acceleration on frequency, at a defined distance, $A_s(f, r)$, is applied to model the excitation term and the site term. The generalized expression in equation (1) can be resolved as below, with the specific parameters, such as geometrical spreading, quality factor, site kappa and seismic moment, explained in the proceeding and following subsections.

$$A_s(r_{ref}, f) = C(2\pi f)^2 M_0 S(f) g(r_{ref}) \exp\left[\frac{-\pi f r_{ref}}{\beta Q_0 \left(f / f_{ref} \right)^{\eta}}\right] \exp(-\pi f \kappa_0) \tag{5}$$

2.3.1 Geometrical spreading and Q

The propagation (or distance) term $D(r, f)$ contains the contributions from the geometrical spreading and anelastic and scattering attenuation.

$$D(r, f) = \log g(r) - \frac{\pi f r}{\beta Q_0 \left(f / f_{ref} \right)^{\eta}} \log e \tag{6}$$

where $g(r)$ is the geometrical spreading function, r is the hypocentral distance, $Q(f)$ is the attenuation function and β the weighted average shear wave velocity of the region. Instead of working directly with this expression in the regression, $D(r, f)$ is initially modelled as a piecewise linear function (Anderson and Lei, 1994; Harmsen, 1997) defined at a frequency f_0 as:

$$D(r, r_{ref}, f) = \sum_{j=1}^{N} L_j(r) D_j(f) \tag{7}$$

where $L_j(r)$ is a linear interpolation function and $\{D_j(f)\}_1^N$ are node values such that $D(r, r_{ref}, f) = D_j(f)$. This definition of the propagation term allows us to model our observations without any *a priori* assumption of the propagation parameters, especially the functional form of $g(r)$. The number of nodes, *n*, is chosen by examining the distribution of observations with distance.

The propagation term $D(r, f)$ is decomposed into $g(r)$ and $Q(f)$ by curve fitting in to the equation (6) and solved as a forward problem. This modelling procedure yields a piece-wise linear geometrical spreading factor as a piecewise continuous function

of distance r^a, which is modelled within a discrete number of distance ranges, to fit the crustal structure of the region.

2.3.2 Source excitation

The excitation term, $EXC(f)$ in equation (1), is interpreted using the Brune (1970) source model from the equation

$$EXC(M_0, f) = C(2\pi f)^2 M_0 S(f); \tag{8}$$

where

$$S(f) = \frac{1}{1 + \left(f / f_c \right)^2}; \tag{9}$$

and

$$C = (0.55)(0.707)(2.0)/4\pi\rho\beta^3 \tag{10}$$

where the density, ρ, shear-wave velocity, β, are for the source depth, and the seismic moment, M_0, is scaled to the reference distance r_{ref} using the attenuation parameters $g(r)$ and Q_0 derived in the first stage. The three values in the numerator of the constant C are nominal values for radiation pattern, average horizontal component and free surface amplification often assumed in stochastic modelling studies (e.g. Atkinson and Boore, 1995).

2.3.3 Site effect

The term $\exp(-\pi\kappa_0 f)$ is used to fit the spectral shape of the excitation function at high frequencies (Anderson and Hough, 1984) and represents the effect of the average site on the source. A network wide average κ_0 is estimated by simply varying its value in equation (5) to obtain the best visual fit to the observed EXC spectrum at high frequencies (e.g., Malagnini *et al.*, 2002). This is a trial-and-error procedure.

3 Data processing and modelling

3.1 Data set

I selected high-quality seismic data by picking seismograms with high signal-to-noise ratio. A high signal-to-noise ratio is defined as when the maximum amplitude is at least three times greater than the RMS value prior to the P arrival. Bandpass filtering is done at a set of central frequencies f_{0i} (i.e. 1.0, 2.0, 3.0, 4.0, 5.0, 6.0, 8.0, 10.0, 12.0, 14.0, and 16.0 Hz). These set of frequencies are the frequencies that have been used in the previous studied in the region. To obtain the filtered time histories around a target frequency f_{0i} I apply a high-pass Butterworth filter (8-pole, $f_{ci} = f_{0i} / \sqrt{2}$) followed by a low-pass Butterworth filter (8-pole, $f_{ci} = \sqrt{2} f_{0i}$). The duration window of the significant part of the filtered seismogram, relative to the central frequency f_0, is then defined as the window bracketing 5% to 75% of the integrated energy. In picking the

coda wave window, I assumed a uniform decay shape of the coda wave, as a function of time, for each seismogram. I picked the start of the coda signal at 20 seconds after the arrival of the S wave. The typical coda time starting at twice the arrival time of the S-wave is approximately 20 seconds for all the events to be used in the study.

3.2 Duration

An estimate of the duration of the signals as a function of distance from the source, for each frequency, is required in order to use Random Vibration Theory to compute the peak values of the filtered time histories, although the method is not used in this study. However, the signal duration is also pertinent in determining the window of picking the coda wave. An over extended duration, beyond the time window for coda, could lead to picking a peak amplitude at a period beyond the coda wave. Such a case would define coda as a wave arriving before the primary signal, or part of the main signal, and therefore misconstruing the entire idea of coda normalization.

Atkinson and Boore (1995) used the duration of the time window that contained the 5-75% fraction of the seismic energy that follows the S-time. Raoof *et al.*, (1999) also found results more consistent with Random Vibration Theory estimates by using the 5-75% duration definition. I also use this predetermined signal duration to constrain the best pick of peak amplitudes in our filtered time histories so as to be consisted with tested methods.

In order to evaluate the sensitivity of our measured peak amplitudes on duration, I analyze the duration variation with distance for different frequencies. I compare the mean duration at different distances for signal duration not exceeding three times the S-wave arrival time with all the events irrespective of the duration time. Figure 3-1 shows some selected frequencies for comparison. The left column are plots for all the events irrespective of the duration time while the right column are plots of events not exceeding three times the S-wave arrival time.

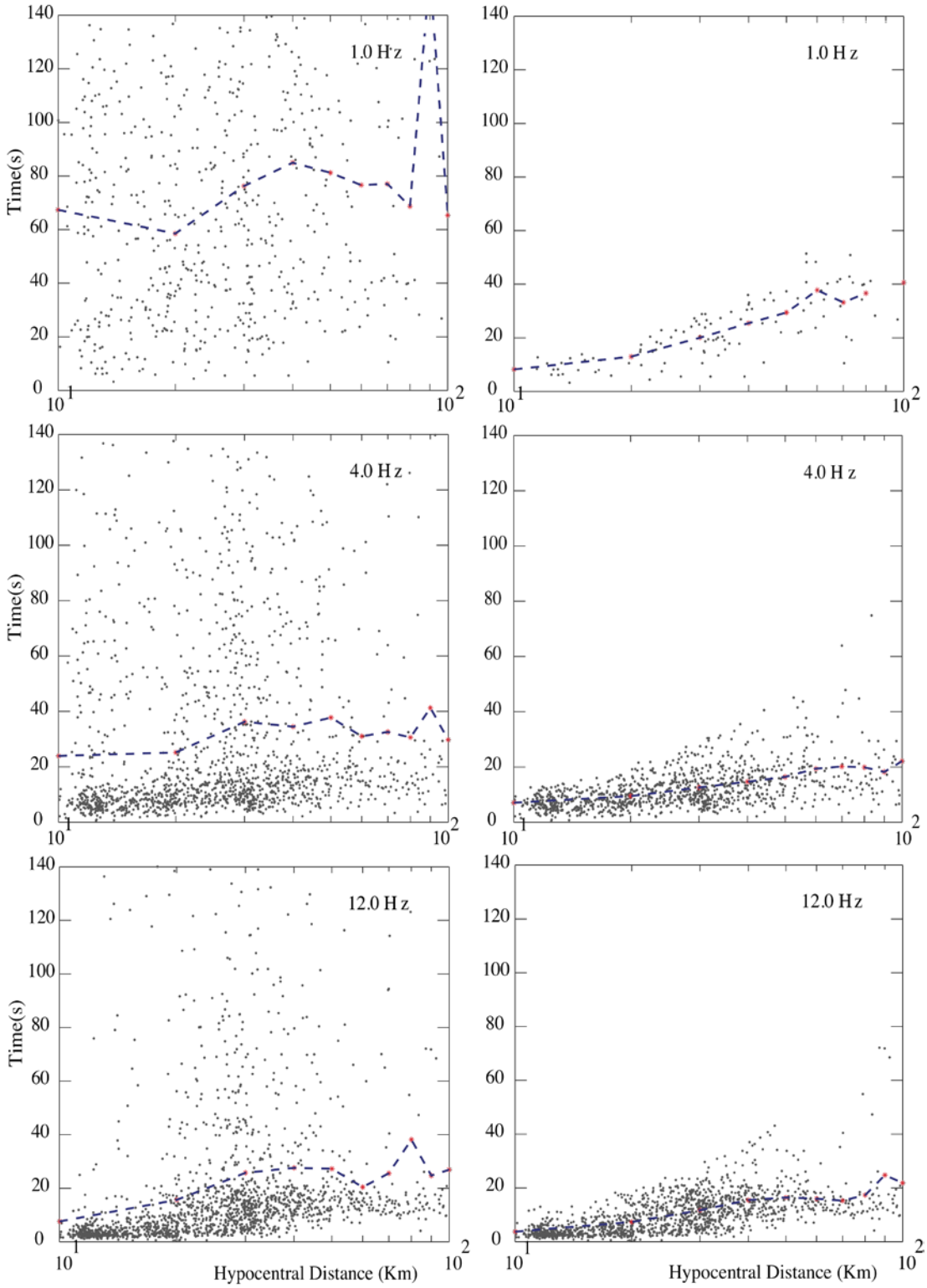

Figure 3-1: Signal duration distribution at 1.0, 4.0, and12.0 Hz obtained for all NMSZ local events (left panel), and for duration not exceeding three times the S-wave arrival time (right panel). The circular points are mean points within the distance bin. The broken line is an interpolation of the mean points.

The fits to the signal duration are shown in Figures 3-1, with the gray dots indicating individual duration estimates, the rounded grey circles are mean duration estimates of individual duration binned at the respective distances, while the dashed lines denote the interpolation of the binned duration estimates. Duration is computed on each individual seismogram as the time window comprising 5-75% of the seismic energy recorded by a specific station. From the left panel, the individual duration estimates (gray dots) show significantly more scatter in the lower frequency range of 1.0 - 5.0 Hz, while the scatter is less at higher frequencies. The number of observations decreases rapidly at large distances and did not permit a reliable estimation of duration at distances beyond 100 km. The durations (thick dashed lines) increase with increasing hypocentral distance and decrease with increasing frequency range. Samiezade - Yazd *et al*. (1996) found similar results. They found signal duration at New Madrid is frequency dependent, with longer durations at lower frequencies.

On the right column, the same data set constrained to signals whose 5 -75% duration do not exceeding three times the S-wave arrival time, provides a scatter with a more linear increase in duration with distance. This trend is consistent across the frequency spectrum with some variation at different distances. The duration variation with distance has previously been modelled by Atkinson and Boore (1995; 2006). The duration is modelled empirically as an increasing function, in a hinged multi-linear fashion from the source, mimicking the form of the attenuation model. The duration could therefore provide a first estimate of the range of the hinged distances in the attenuation model of the region.

There is a clear difference in the change of the durations in the lower frequency range of 1.0 Hz to 5.0 Hz. The higher level of scatter could have been influenced by noise. The higher frequencies are robust and unaffected by the constraint and therefore provide a stable basis for modelling the distance term. I therefore use only the shorter duration signal in the following analysis at frequencies below 6 Hz. However, the use of all the signals irrespective of the extent of duration should provide the same results at frequencies above 6 Hz.

3.3 The distance term D

3.3.1 Initial estimate of D

The initial estimate of the distance term is performed in stages. First is the binning of the normalized amplitude at different distances in order to find a mean amplitude representative at that distance. The second step in the process is interpolation of the binned amplitudes with distance. The interpolation of mean amplitude provides a graph of the attenuation function that can be interpreted visually to determine the hinges of the geometrical spreading. The third step in the process is a multi-linear fit of the interpolation to find the best-fit equation. The above three –step process is applied to each frequency separately then the results are combined together for forward modeling.

Figure 3-2 is an example of the process of the initial estimate of D for a normalized time series filtered at 8.0 Hz (for other frequencies refer to the appendix). The top left panel shows the coda-normalized peak velocity distribution estimated using the coda normalization technique. The line interpolates between the mean points binned within a distance window. The top right shows a bilinear cubic least-square fit (CLS fit) of the interpolation, while bottom panel shows the residuals of the regression analysis.

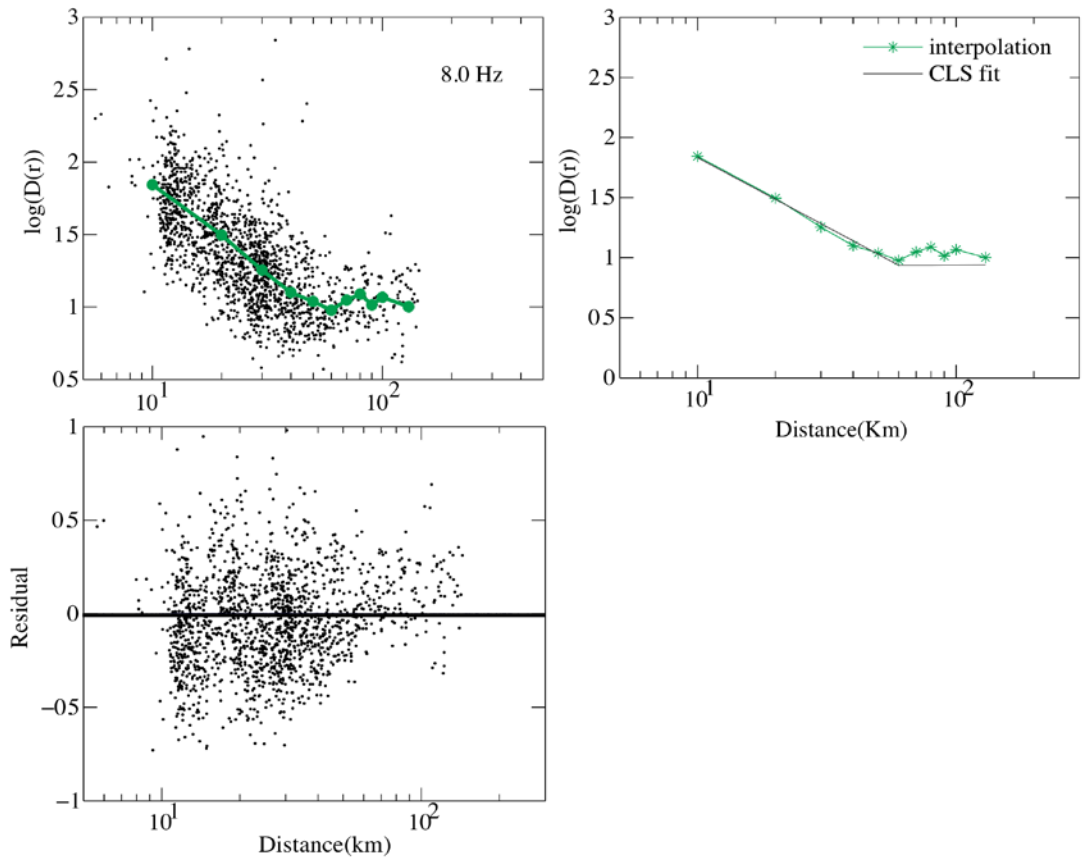

Figure 3-2: Regression of coda-normalized peak velocities at 8.0 Hz obtained for NMSZ local events. The gray dots indicate individual normalized peak estimates, the rounded coloured circles are mean peak estimates of the individual peaks binned at the respective distances, and lines denote the different fitting lines of the binned duration estimates. Top left - the coda-normalized peak velocity distribution; Top right - bilinear cubic least-square fit of the interpolation; Bottom - residuals of the regression analysis.

3.3.2 Forward modelling

The results from the initial estimate of D above are then used for the forward modelling of the final distance term. The forward modelling process breaks-up the distance term into geometrical spreading and quality factor values to be used in inversion of the excitation. I achieve this by first fitting the geometrical spreading of a body wave to the distance before the cross-over distance, to determine the quality factor. I then apply the quality factor to establish the geometrical spreading of the other distance portions using equation (11), to produce Figure 3-3 as an example of a forward model of normalized time series filtered at 8.0 Hz, as used in the proceeding section,

$$D(r,f) = \log g(r) - \frac{\pi f r}{\beta Q_0 \left(f / f_{ref} \right)^{\eta}} \log e \tag{11}$$

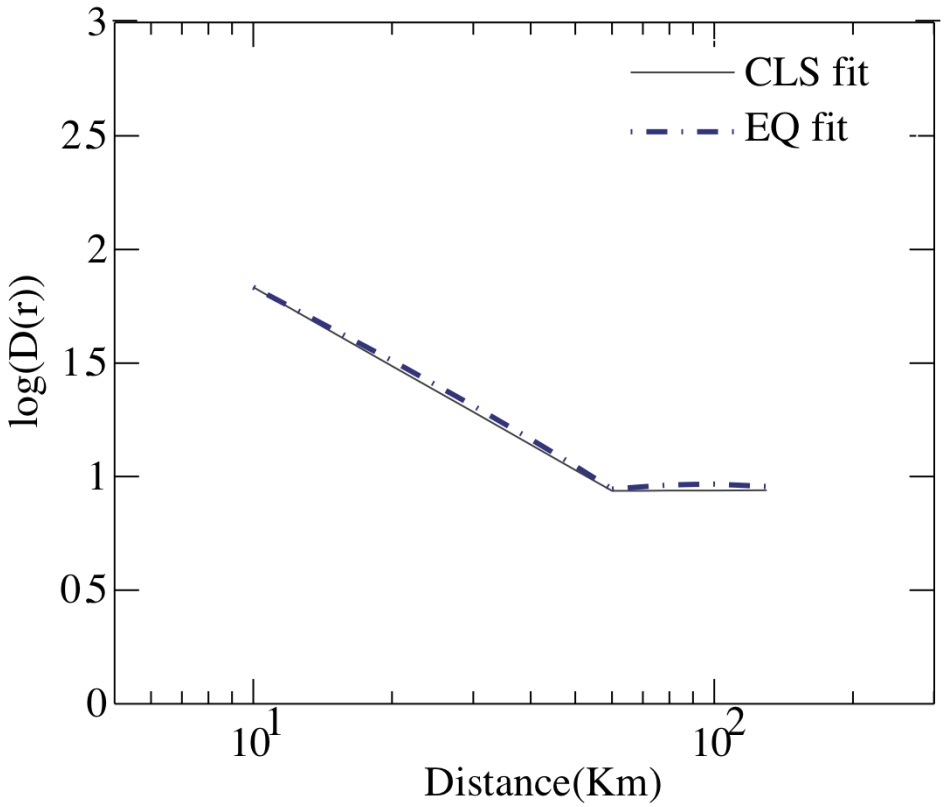

Figure 3-3: A forward model (broken line) of a least-squares fit (solid line) for the attenuation function of normalized time series filtered at 8.0 Hz.

I initially solve for the average attenuation of the region irrespective of the style-of-faulting including normal fault events, and events whose focal mechanism were not defined, then solve separately for the strike slip events and reverse events, and finally compare and contrast the attenuation results. I note that two of the parameters of the propagation function trade-off with each other. Specifically the rate of geometrical attenuation (e.g. 1/r) trades-off with the attenuation function $Q(f)$. In any modeling exercise we must choose a measure of misfit that can be used to favor one set of model parameters over another.

3.3.3 Average attenuation

The NMSZ produced an average geometrical spreading of

$$g(r) = \begin{cases} r^{-1} \; ; & r \le 60km \\ r^{0.5} \; ; & 60km < r < 130km \end{cases}$$

and an attenuation function

$$Q(f) = 660\, f^{0.35}$$

using a shear wave average velocity of 3.6 km/s.

A spherical spreading of body waves resulting in an r^{-1} amplitude decay, fits within a 60 km distance, with an attenuation function $Q(f)$ of $660\, f^{0.35}$. Beyond the 60 km distance the amplitude increases at the rate of $r^{0.5}$ as indicated in figure 3-4.

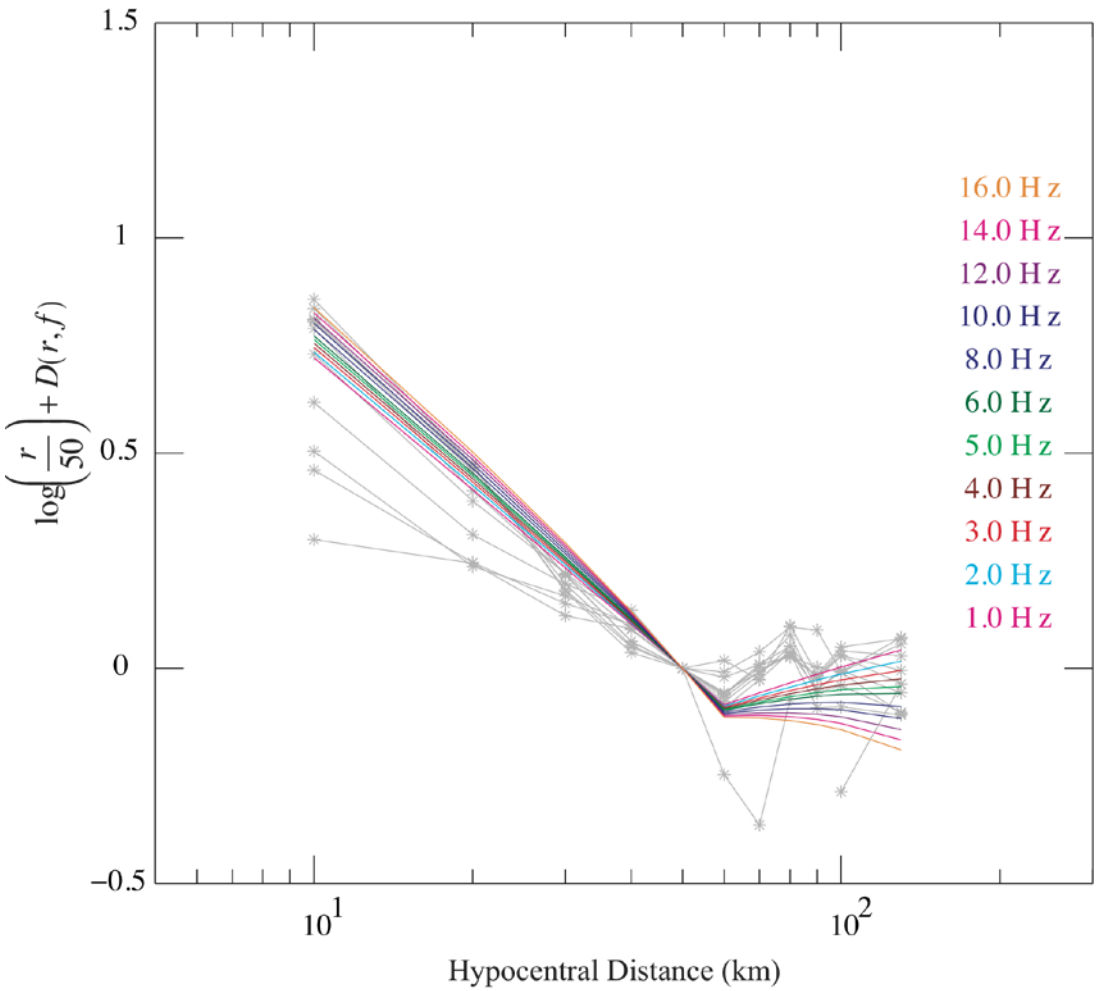

Figure 3-4: Attenuation functional obtained from the regression of the filtered velocities. Colored tones represent the final regression, the gray lines in the background describe the interpolation of mean-points of binned amplitude within a distance window. The reference hypocentral distance is 50 km.

In the ENA region, the geometric attenuation of seismic waves, in previous studies, is given by a three-part expression. Atkinson and Mereu (1992) used 1500 seismograms from 100 earthquakes and found the spectral-amplitude decay due to

geometric spreading being approximately independent of frequency. Their best fit to the data gave a tri-linear geometrical spreading hinged at 70 km and 140 km. The first 70 km, they found an amplitude decay of $r^{-1.1}$ followed by no apparent geometric spreading in the intermediate distance. For distance greater than 130 km, geometric spreading was modelled as $r^{-0.5}$ with an associated $Q(f)$ model of $670 f^{0.33}$. Alternatively, by assuming a bilinear form (r^{-1}, $r^{-0.5}$, $Q(f)^{\eta}$) the model fit well if the transition from direct wave to Lg spreading was placed at approximately 60 km. this means that the choice of geometrical spreading was much more dictated by the preferred attenuation model. The first distance portion of the bilinear model is identical to the results in this study. This study has more data set within the first 100 km than Atkinson and Mereu's study and therefore provides a better constrain on the modelled geometrical spreading. The $Q(f)$ values are significantly similar with the difference may be due to the different frequency spectrum considered in the two studies (i.e. 1, 2, 4, 8 Hz for Atkinson and Mereu, 1992) to provide refined results.

Atkinson and Mereu's study provided a starting point for Atkinson and Boore (1995) to produce an improved model by making some adjustments. Their model had a geometrical spreading of r^{-1} in the first 70 km, which is consistent with my model except for the distance range. The other distance segments retaining the values in the starting model. The quality factor derived by refitting the data of Atkinson and Mereu (1992) increased to $680 f^{0.36}$, to provide a wider margin as compared to my results. This difference can be attributed to the low attenuating nature of the Canadian Shield compared to the Mississippi Embayment. The low attenuation is even more explicit in new ENA ground-motion prediction equations for hard-rock produced sites by Atkinson and Boore (2006) based on a stochastic finite- fault model. The model had an associated Q of $893 f^{0.32}$ in their study, they found the geometric spreading was significantly faster at near-source distances (70 km) than was determined in previous studies. The Fourier amplitudes decayed as $r^{-1.3}$ within 70 km of the source, then increased as $r^{0.2}$ in the intermediate distance. This increase was attributed to Moho bounce effects, and has been experienced in this study. The amplitudes then decreased as $r^{-0.5}$ beyond 140 km. the difference in amplitude decay could be due to the type of data set considered in analysis. Atkinson and Boore (2006) use Fourier amplitudes, which could be lower at greater distances compared to time series due to the extended duration nature of the time series.

In this study, to fit a 70 km body wave geometrical spreading, the data set requires a $r^{-0.9}$ amplitude decay with a corresponding attenuation function $Q(f)$ of $960 f^{0.35}$. To fit a geometrical spreading of r^{-1} within the 70 km distance, an intrinsic attenuation of Q >1000 is required to fit our data set (Appendix B). Moreover, by having the data set dictate the empirical fit of the attenuation function, there is a clear change of geometrical spreading observed at 60 km hypocentral distance, a characteristic observed in the plot of duration. The departure of this distance factor from the previous attenuation models could be due to a proposed high velocity rift pillow, lying above the Moho within Mississippi Embayment, which could reduce the crustal thickness hence travel time of critically refracted rays producing pseudo-Moho post-critical reflections at a shorter

distance. Despite the difference in the distance for the change of geometrical spreading in these previous studies, there is a general consensus on the geometrical spreading for at least the first 50 km.

Samiezade - Yazd *et al*. (1996) performed a regional comparison of vertical ground motion in the NMSZ. They used a seismic data set consisting of vertical component recordings from the Cooperative New Madrid Seismic Network, and from the PANDA New Madrid deployment. Using the same method used in this study, they found signal duration was frequency dependent due to variability of duration and geometrical spreading with distance, an attribute that is evident in this study. They conceded it was difficult to obtain Q from the time domain observations. Nevertheless, they applied a Random Process Theory modelling to estimate and fit the New Madrid data sets. Although they don't indicate how they determine the attenuation parameters, they came up with a Q of $Q(f) = 900 f^{0.3}$ with a geometrical spreading varying as r^{-1} within 0-50 km, $r^{-0.25}$ within 50–120 km and r^{0} within 120–500 km. These results differed from our finding with a larger Q value and different hinge distances for different geometrical spreading. One of the reasons for the difference could be the data used. Samiezade - Yazd *et al*. use the S wave in the vertical component of the seismogram. The vertical component does not represent the true horizontal motion and might not provide the absolute motion in that sense. This current study uses the horizontal component seismograms with improved number of events, nearly four times although with fewer stations, to achieve more improved results. There is a clearly visible trend in the amplitude decay with distance, which permits a decisive choice of the geometrical spreading and Q, to provide a Q that is consistent with the values arrived at by Atkinson and Mereu (1992) and Atkinson and Boore (1995).

3.3.4 Attenuation for different styles-of-fault

Modelling of the attenuation function for the different styles of faulting produces two different results. I performed the analysis to estimate the distance term, using the previously discussed procedure, for strike slip and reverse fault events separately. Using a common quality factor, the forward models for the two styles of faulting provide two distinct models of geometrical spreading. Figure 3-5 is an illustration of the variation between the attenuation of reverse fault events and strike-slip events compared to the average attenuation at different frequencies. The events are modelled up to 60 km due to scarcity of the records beyond the distance. At frequencies below 5 Hz, the number of records is not sufficient to produce successive bins for least-square fitting.

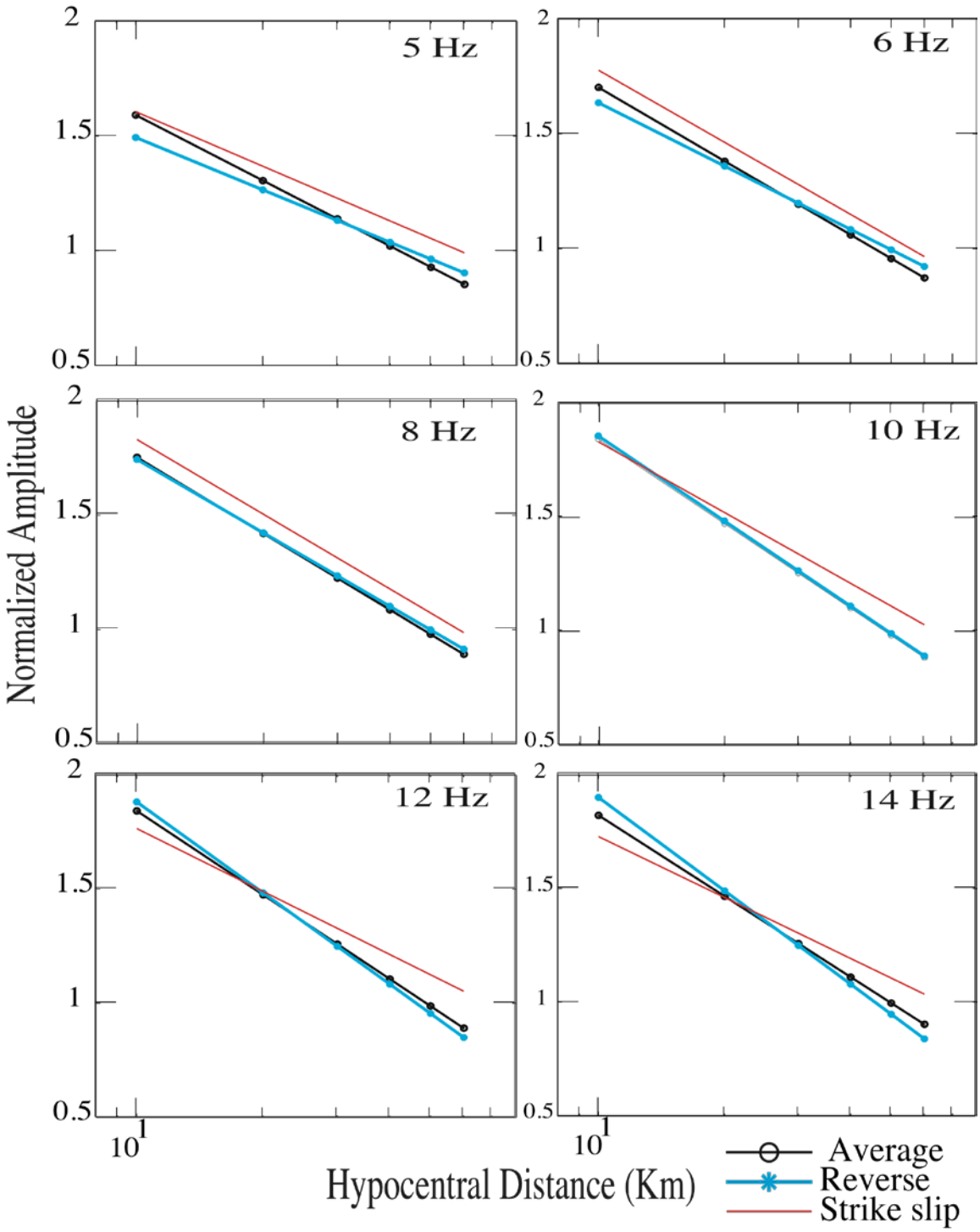

Figure 3-5: Linear cubic least-square fit of interpolated normalized amplitudes for all events combined (average), reverse fault events (Reverse) and strike slip fault events (Strike slip) at different frequencies.

From the analysis, the reverse fault events have a higher ground motion near the source, at frequencies more than 8 Hz, and also have a faster decay of the amplitude with

distance than the strike-slip fault events. Apart from the slight difference at 6 Hz, the attenuation for the two styles of faulting is similar at 8 Hz and below. Comparing to the average attenuation of the region, reverse fault events have a body wave geometrical spreading of $r^{-1.1}$. This translates to a 10% increase on the geometrical spreading factor. On the other hand, strike-slip events provide a body wave geometrical spreading of $r^{-0.75}$ on the lower end. This provides a 20-35% difference between the reverse fault and strike-slip amplitude decay with distance. At lower frequencies, no difference is discerned for the two styles of faulting. Although the statistical significance of this difference has not been calculated, the observed difference cannot be ignored.

Considering the small size of these events in NMSZ, the source functions are interpreted to have a circular fault area and as point sources. The statistical nature of this analysis minimizes the possibility of that directivity produces the difference in attenuation between strike slip fault events and reverse fault events, since the ground motions are averages over the region irrespective of the azimuth of the recording stations. The difference in attenuation may be attributed to the radiation pattern of the two styles of faulting.

Narayan (2001) determined that radiation pattern differences could create higher displacement amplitude for reverse faults near the seismic source compared to the strike slip fault. However, the reverse fault wave propagation is only close to the source compared to strike slip fault especially on the transverse component. Even though Narayan's simulation introduces a dip of 90^0 for strike slip fault and 10^0 for reverse fault, the radiation pattern of body waves for a point shear dislocation (figure 3-6) indicates an increase in magnitude with reduction in emergence angle of the horizontal shear wave of a strike slip style of faulting. High-angle reverse faults dipping varying from 60° to 80° have high amplitudes near the source that decrease with distance. A cross-over between strike slip and reverse is observed at ~130^0, corresponding to ~20 km for a point source at 8 km depth. This distance coincides with the one observed at 12 Hz in figure 3-5. Radiation pattern can explain the near source difference in ground motion amplitudes observed in our study for strike-slip and reverse faults.

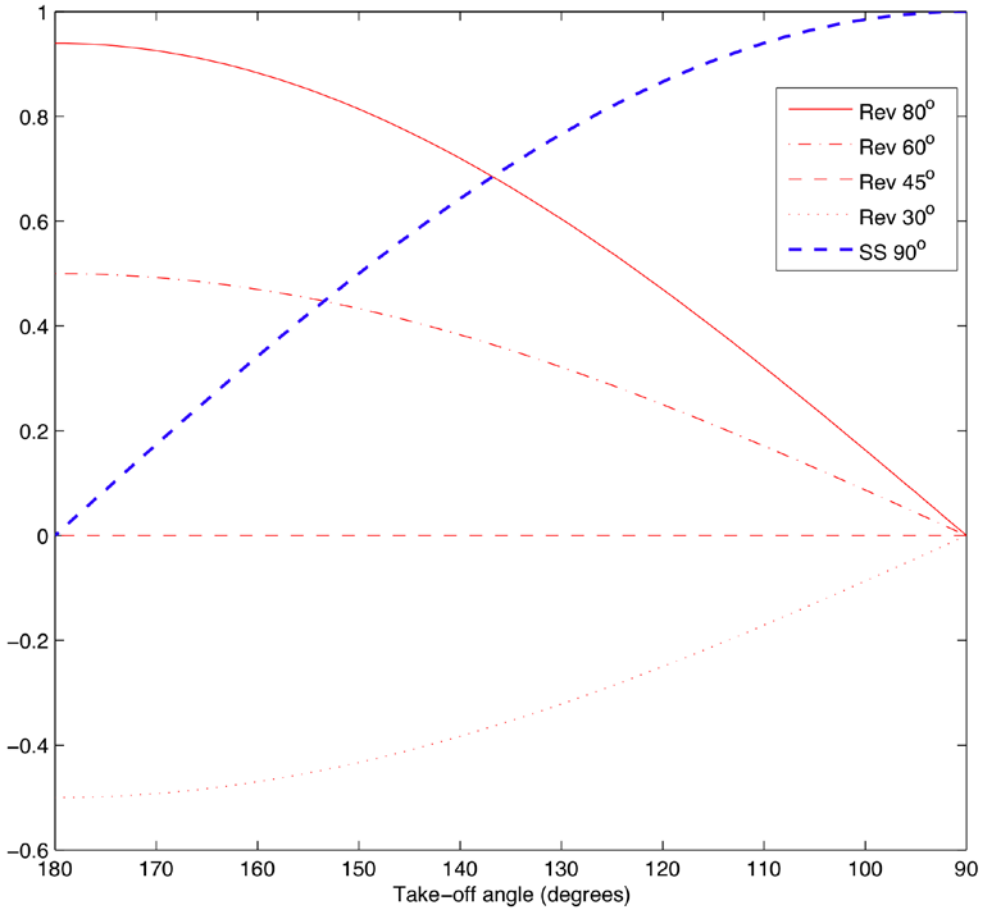

Figure 3-6: Variation of take-off angle of the dimensionless form of radiation pattern of body waves for strike slip faulting and reverse faulting. The reverse faulting is considered at different angles of dip (i.e. in the legend).

3.4 Excitation

The excitation term provides source parameters such as seismic moment (M_0), static stress drop $(\Delta\sigma)$, corner frequency (f_c) and fall-off frequency $(f_{\max})$. The seismic moment can be obtained from long period levels of the displacement spectra or acceleration spectra. We compare both the displacement spectra and acceleration spectra to obtain the corner frequency estimate. The fall-off frequency and kappa are determined from the acceleration spectra. The stress drop, which controls the strength of the high frequency radiation, can either be determined using the radius of circular crack model (r), or corner frequency using the expressions below (Brune 1970,1971; Hanks and Thatcher 1972).

$$\Delta\sigma = \frac{7}{16}\frac{M_0}{r^3} \tag{12}$$

or

$$\Delta\sigma = 8.47 M_0 \left(\frac{f_c}{\beta} \right)^3 \tag{13}$$

I interpret the excitation of different magnitude events in NMSZ based on the Brune source model. Using the acceleration spectra, we are able to easily identify the fall-off frequency and fit the kappa value using the theoretical excitation equation 5. Excitation is modelled at the closest distance (i.e. 10 km) to the source where it is less susceptible to intrinsic attenuation and before the change of radiation pattern from body wave geometrical spreading. The attenuation properties applied in this model are those derived in the distance model above. Using events with moment magnitude indicated in the catalogue, I validated the equation to find the seismic moment of events expressed in duration magnitude.

Figure 3-7 and 3-8 shows the spectral fitting of a moment magnitude 3.5 earthquake source spectra as an example. In gray are the smoothed source spectra of different events of equivalent duration magnitude, while the dashed and solid curves are spectral fitting of source model for different values of κ_0 (kappa). The spectral fitting of the excitation term produced an estimate kappa value of 0.011± 0.004. This kappa value has been estimated for many events recorded by the network and represents an average of the region. The fall-off frequency $f_{\max}$ is observed at ~30 Hz across the region.

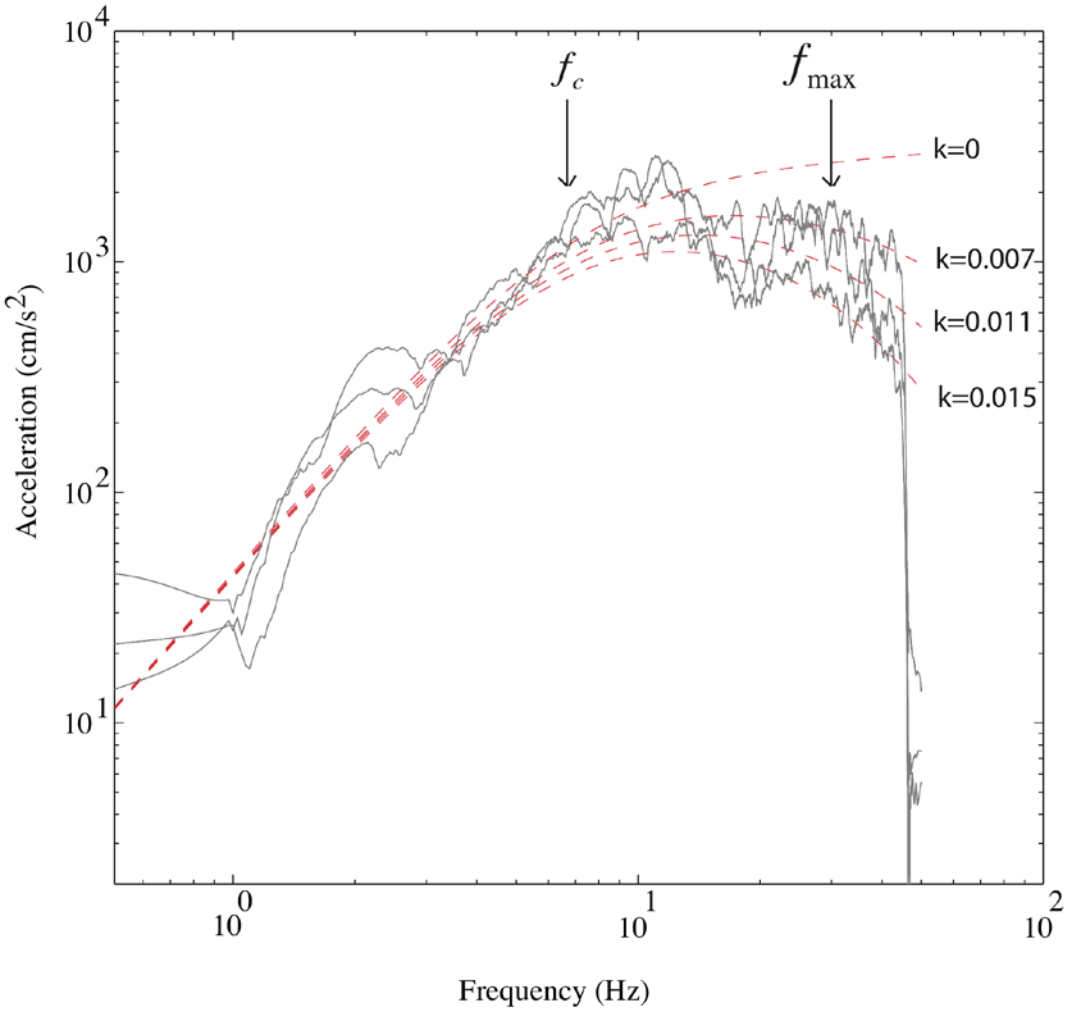

Figure 3-7: Acceleration spectra fitting using a Brune's source model for moment magnitude 3.5 earthquakes in NMSZ indicating the pick of f_c and f_{max}.

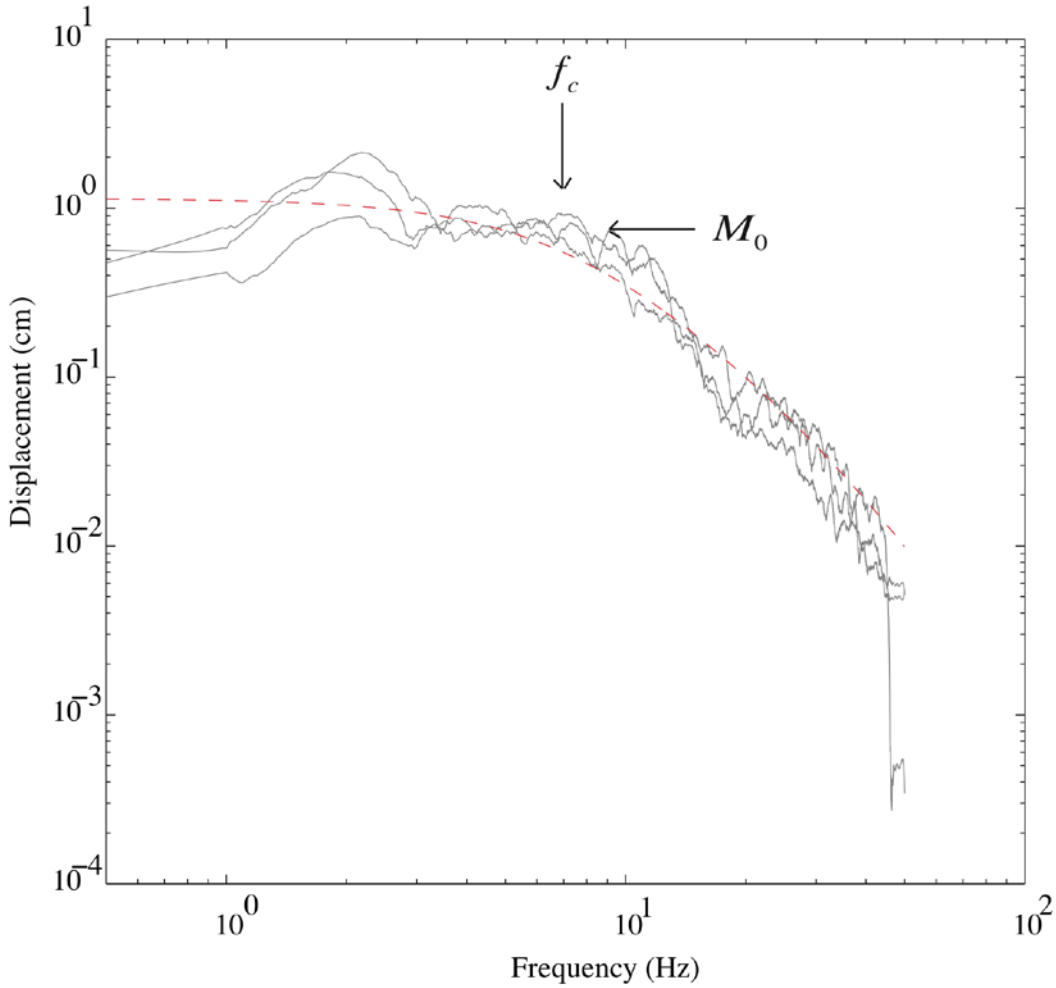

Figure 3-8: Displacement spectra fitting using a Brune's source model for duration magnitude 3.5 earthquakes in NMSZ indicating the pick of f_c and M_0.

The κ_0 value 0.011± 0.004 is in agreement with the 10 msec used by USGS to adjust hard-rock ground motions to National Earthquake Hazard Reduction Program (NEHRP) BC site profiles (sediment plus hard rock) in the Mississippi Embayment (Petersen *et al*. 2008). Whereas, Atkinson and Boore (1995) and Campbell (2007) used 20 msec in the development of their BC ground-motion prediction equations, a value arrived at recently by Campbell (2009). Campbell (2009) found κ_0 to increase linearly with the thickness of the sediments with estimated values for the BC section of the sedimentary column ranging from as low as 4 msec for a 116 m thick column to as high as 26 msec for a 600 m thick column. κ_0 can be interpreted in terms of sediment Q_s. For a sedimentary profile of a given thickness, κ_0 can expressed as (Boore, 2003)

$$\kappa_0 = \frac{H}{\overline{Q_s}\,\overline{V_s}} \tag{14}$$

where H is the sediment thickness. Using the above expression, the median value of κ_0 in this study translates to sediment Q_s of 90. This value applies to the unconsolidated sediments (~600 m thick) overlying Paleozoic rock in the NMSZ. Some previous studies have provided Q_s values as low as 10–30 for the upper 30 m of the sediments (Wang *et al.* 1994), with a recent vertical seismic profiling study (VSP) by Pujol *et al.* (2002) yielding 22–34 for Q_s for the upper 60 m. These much lower Q estimates are for the top sediment layer and are not directly comparable to the Q value determined in this study. However, Langston *et al.* (2005) found sediment Q_s of 100, which concur with my values, and are complemented by a high fall-off frequency to indicate near-surface low attenuation.

3.4.1 Duration magnitude and Moment magnitude

Moment magnitude (Mw) is the preferred magnitude for seismic hazard analysis, and determining how other magnitude scales are related to it is important, as Mw estimates are not always available. The inversion of source spectra, in the preceding section, provides the seismic moment for each seismic event to calculate the moment magnitude. I then determine how duration magnitude relates to moment magnitude using 119 events in the Cooperative New Madrid Seismic Network (CNMSN) catalogue. Figure 3-9 is plot of duration magnitude against moment magnitude on top, and the residual of the least squares fit on bottom. The solid line is a least-squares fit of the data set. It shows that the average relation between M_W and M_D (for $1.6 \leq M_D < 3.0$) is $M_W = 0.7344M_D + 0.9411$.

Although the maximum difference between M_D and M_W may get as large as ~1 magnitude unit, the average difference is very small. The residual plot shows an even distribution of the data around the least square fit especially for the events of $M_D \leq 2.5$. Above $M_D = 2.5$ the data is on the lower side of the equation. This would seem to indicate another possible relationship within the magnitude margin. This can be verified by addition of more data set within $2.6 \leq M_D < 3.0$. This magnitude relationship is relatively similar to Miao and Langston (2007). They used 27 events to find a relationship between local magnitude and moment magnitude, as well as 594 events to find a relationship between duration magnitude and local magnitude. Using their two relationships, i.e. $M_W = 0.7603M_L + 0.817$ and $M_L = 1.008M_D + 0.0714$, the study provides $M_W = 0.7672M_D + 0.8713$.

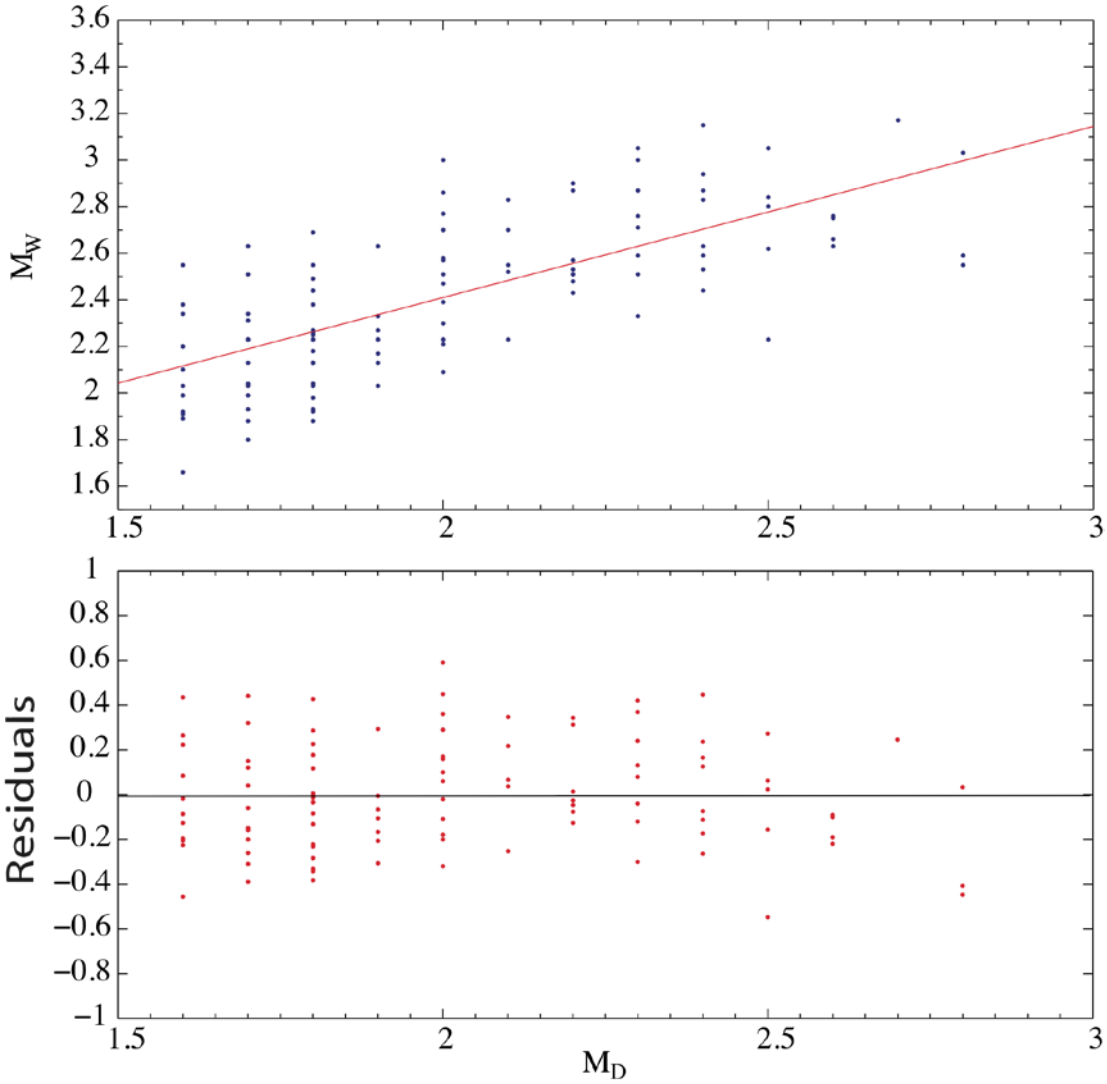

Figure 3-9: Relationship between M_W and M_D for the NMSZ based on 119 events occurring from 2000 to 2007 (top), and the residuals of the least squares fit of the regression (bottom). The average relation between M_W and M_D is $M_W = 0.7344M_D + 0.9411$.

3.4.2 Stress drop

In determining the stress drop, I inverted for the seismic moment using the excitation equation (12) by averaging over stations within 60 km from the source for each event. I used both the acceleration spectra and displacement spectra to find the best constraint of the corner frequency. The stress drop values were calculated using a velocity model (table 3-1) developed by Chiu *et al.* (1992). I used 11 events having $M_W > 3$ already calculated in the catalogue, listed in Table 3-2 along some source parameter approximations, and 119 events of $M_D < 3$.

Table 3-1 NMSZ crustal model from Chiu *et al.* 1992.

Thickness (km)	P Velocity (km/sec)	S Velocity (km/sec)
0.65	1.8	0.6
1.85	6.02	3.56
2.5	4.83	3.2
12.0	6.17	3.57
10.0	6.6	3.8
13.0	7.3	4.2

The comparison of stress drop with seismic moment is plotted in figure 3-10. Crosses represent the 11 events in table B-3 while the other events are shown by coloured dots with blue for reverse faulting and red for strike slip faulting events. The figure (3-10) indicates an increasing trend of stress drop with seismic moment up to M_W= 3.5 beyond which the stress drop varies between 100 bar to 165 bar. The mean stress drop for $M_W \geq$ 3.5 events is 138 bar. This mean is comparable to the 140 bar median stress drop inferred by Atkinson and Boore (2006) using updated set of ENA seismological parameters along with a finite-source stochastic simulation model (EXSIM) for eight instrumentally recorded events.

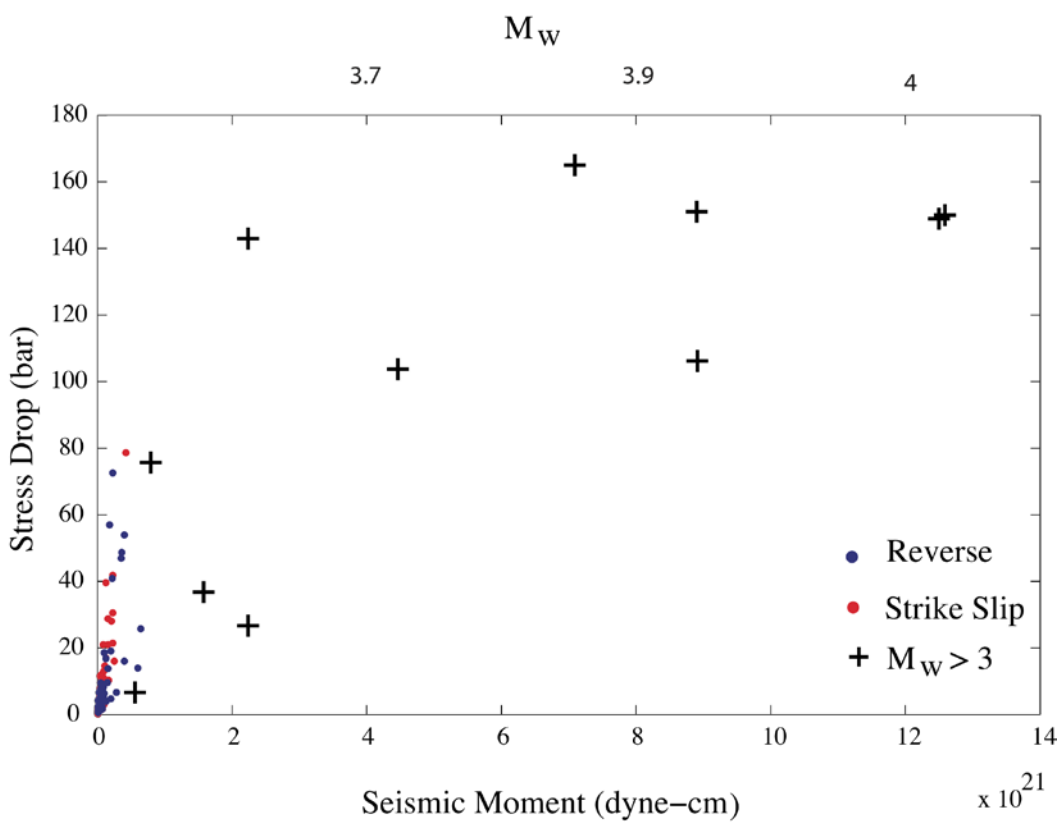

Figure 3-10: A plot of Seismic moment vs Stress drop for 130 events in NMSZ

Figure 3-10 is re-plotted (figure 3-11) in logarithmic scale to better view the low magnitude events. The plot indicates a linear increment of stress drop with seismic moment for $M_W < 3.5$ events. The fall-off frequency, f_{max}, for earthquakes in the NMSZ is close to 30 Hz. Above 30 Hz then site attenuation may lower the corner frequency estimate. For a constant stress drop of 140 bars, a corner frequency of 30 Hz is expected for an M_W =2.3 earthquake. So the corner frequency and stress drop estimates should be reliable for earthquakes with M_D >2.3. Since this increase in stress drop with increasing seismic moment is observed in figure 3-10 for earthquakes with M_D >2.3, the observation requires further investigation. This phenomenon is complex and raises many questions. A dedicated study can be done to understand this characteristic.

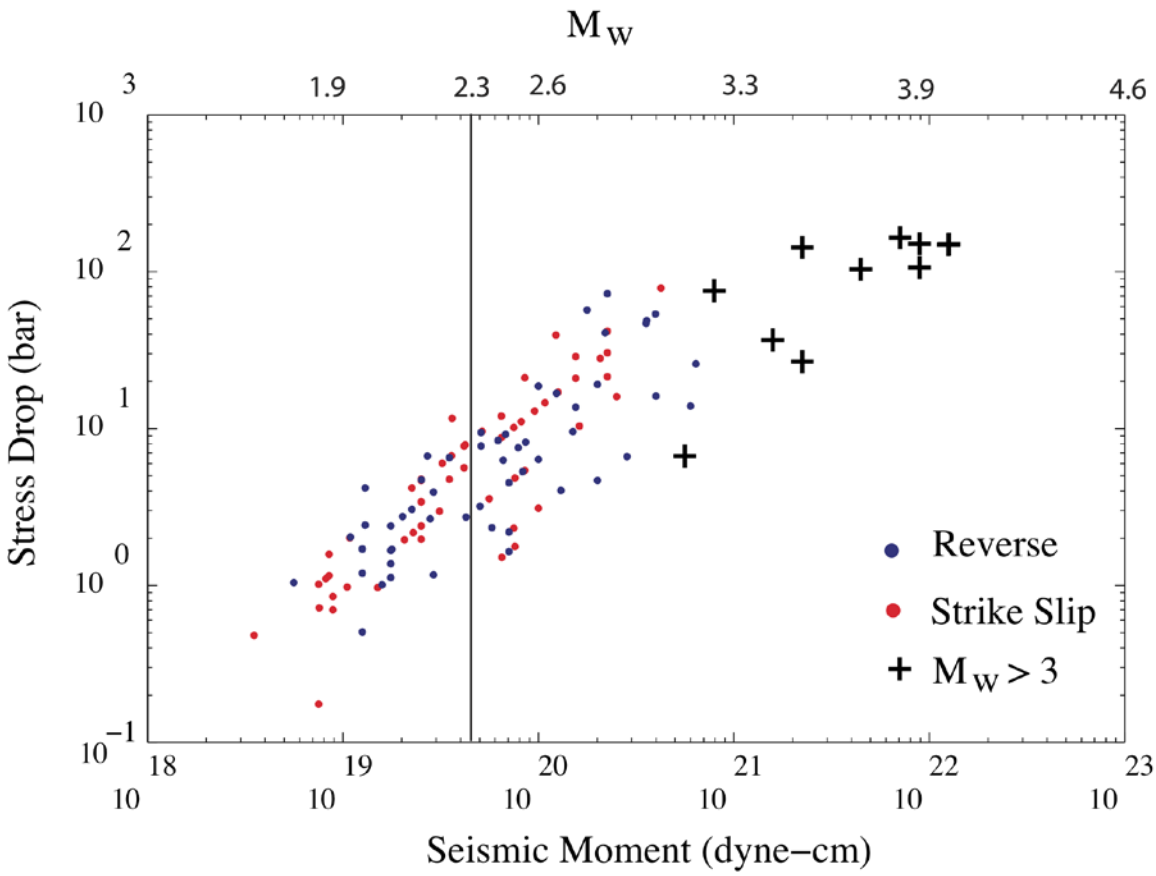

Figure 3-11: A logarithmic plot of Seismic moment vs Stress drop for 130 events in NMSZ

4 Conclusion

I have investigated the effects of style of faulting on earthquake ground motion in the New Madrid Seismic Zone (NMSZ) by analysing local waveform data using a multistage processing method, successfully used by Raoof *et al.* (1999) and Malagnini *et al.* (2000), to produce empirical attenuation relations for a band of narrow frequencies centred at 1, 2, 3, 4, 5, 6, 8, 10, 12, 14 and 16 Hz. Using seismic data from the year 2000 to 2009, 854 seismic events provided quality data, by our definition, and in conjunction with earthquake focal mechanisms from two recent studies (Johnson *et al.*, 2008; and Horton, 2008), I produced attenuation models and some source parameters for strike slip and reverse fault Earthquakes.

The seismic signal was susceptible to noise at frequencies below 5 Hz. This is clearly seen in the distribution of duration with distance. At frequencies above 5 Hz, the duration of the signal increases with distance with most of the durations below 20 sec. The attenuation analyses yield a bilinear geometrical spreading relationship within 135 km of hypocentral distance. The analytical results, based on the frequencies larger than 5 Hz, provide a regional average geometrical spreading of r^{-1} with a quality factor of $Q(f) = 660 f^{0.35}$ within the first 60 km hypocentral distance. Beyond 60 km distance, the geometrical spreading changes to $r^{0.5}$. An increase in amplitude beyond 70 km has been observed in eastern North America and attributed to Moho bounce effects by Atkinson and Boore (2006). The 60 km distance range for the change of geometrical spreading does not coincide with the regional Moho depth. I suggest this change in geometrical spreading may be due to a high velocity rift pillow, proposed to lie above the Moho within Mississippi Embayment.

The attenuation results considering different style of faulting indicate a faster decay of the amplitude with distance for reverse fault events than for strike-slip fault events in the region. This difference is found at frequencies greater than 8 Hz. The amplitude decays as $r^{-1.1}$ and $r^{-0.75}$ for reverse and strike-slip events respectively, to provide a 20-35% difference between the two styles of fault near the source. This difference may be due to differences in radiation pattern for strike-slip and reverse faults. At lower frequencies, no difference is discerned for the two styles of faulting.

The source function produces an estimate of kappa value of 0.011± 0.004 with regional fall-off frequency $(f_{\max})$ of observed at ~30 Hz, indicating that unconsolidated and semiconsolidated sediments of the embayment might not significantly attenuate low-strain earthquake ground motions.

The study provides a mean stress drop of 135 bar for events with a moment magnitude greater than 3.5. At lower magnitude, the stress drop increases with linearly with seismic moment. With no justified explanation for this observation, it provides an insight for future studies.

4.1 Future studies

The attenuation results produce a model with a hypocentral distance limit of 135 km, this study can be expanded to cover the larger region of ENA so as to illuminate on how the radiation pattern varies beyond 135 km, especially with the advent of USArray. Since lower frequencies had longer energy duration and did not provide desired results, a better understanding of these frequencies is needed. A similar study can be done in

central Arkansas, where the effect of sediment is subtle, to provide a comparison besides an attenuation model.

In this study the stress drop for small magnitude earthquakes seems to increase with increasing seismic moment. This is important for earthquake source scaling in eastern North America, and a more dedicated study should be done in order to the unknown properties of these small events.

Reference

Aki, K. (1969), Analysis of the Seismic Coda of Local Earthquakes as Scattered Waves, *J. Geophys. Res.* **74**, 6215-6231.

Aki, K. (1980). Attenuation of shear waves in the lithosphere for frequencies from 0.05 to 25 Hz, *Phys. Earth Planet. Inter.* **21**, 50-60.

Aki, K. and Chouet, B. A. (1975). Origin of coda waves: source, attenuation and scattering effects, *J. Geophys. Res.* **80**, 3322-3342.

Anderson, J. G. and S. E. Hough (1984), A model for the shape of the Fourier amplitude spectrum of acceleration at high frequencies, *Bull. Seism. Soc. Am.* **74**, 1969-1994.

Anderson, J. G. and Y. Lei (1994). Nonparametric description of peak acceleration as a function of magnitude, distance, and site in Guerrero, Mexico, Bull. *Bull. Seism. Soc. Am.* **84**, 1003-1017.

Atkinson G. M. (1984). Attenuation of strong ground motion in Canada from a random vibrations approach, *Bull. Seism. Soc. Am.* **74**, 2629-53.

Atkinson, G. M. and D. M. Boore (1990). Recent trends in ground motion and spectral response relations for North America, *Earthquake Spectra* **6**, 15-35.

Atkinson, G. M. and D. M. Boore (1995). Ground motion relations for eastern North America, *Bull. Seism. Soc. Am.* **85**, 17-30.

Atkinson, G. M., and D. M. Boore (2006). Ground motion prediction equations for earthquakes in eastern North America, *Bull. Seism. Soc. Am.* **96**, 2181-2205.

Atkinson, G. and R. Mereu (1992). The shape of ground motion attenuation curves in southeastern Canada, *Bull. Seism. Soc. Am.* 82, 2014-2031.

Autin, W. J., Burns, S. F., Miller, B. J., Saucier, R. T., Snead, J. I. (1991). Quaternary geology of the Lower Mississippi Valley. In: Morrison, R. B. (Ed.), Quaternary Nonglacial Geology; Conterminous US Geological Society of America, The Geology of North America, Vol. K-2. Boulder, CO, pp. 547–58.

Beresnev, I. A. and G. M. Atkinson (1998). "FINSIM - a FORTRAN Program for simulating stochastic acceleration time histories from finite faults, *Seismol. Res. Lett.* **69**, 27-32.

Bertagne, A. J., and T. C. Leising (1991). Interpretation of seismic data from the Rough Creek graben of western Kentucky and southern Illinois, in *Interior Cratonic Basins: American Association of Petroleum Geologists Memoir 51*, M. W. Leighton, D. R. Kolata, D. F. Oltz, and J. J Eidel (Editors), *AAPG*.

Bickford, M. E., W. R. Van Schums, and I. Zietz (1986). Proterozoic history of the midcontinent region of North America, *Geology* **14**, 492-496.

Boore, D. M. (1983), Stochastic simulation of high-frequency ground motions based on seismological models of the radiated spectra, *Bull. Seism. Soc. Am.* **73**, 1865-1894.

Boore, D. M. (2002). SMSIM Fortran programs for simulating ground motions from earthquakes: Version 2.16. A revision of OFR 96-80-A. Menlo Park, US Geological Survey.

Boore, D. M. (2003). Prediction of ground motion using the stochastic method, *Pure Appl. Geophys.* **160,** 635-676.

Boore, D. M. and G. M. Atkinson, (1987). Stochastic prediction of ground motion and spectral response parameters at hard-rock sites in eastern North America, *Bull. Seism. Soc. Am.* **77**, 440-467.

Brune, J. N. (1970). Tectonic stress and the spectra of seismic shear waves from earthquakes, *J. Geophys. Res.* **75**, 4997-5009.

Brune, J. N. (1971). Correction, *J. Geophys. Res.* **76**, 5002.

Burke, K. and J. F. Dewey (1973). Plume-generated triple junctions: key indicators in applying plate tectonics to old rocks, *Journal of Geology* **81**, 406-433.

Campbell , K.W. (2009). Estimates of Shear-Wave Q and k_0 for Unconsolidated and Semiconsolidated Sediments in Eastern North America. *Bull. Seism. Soc. Am*. **99**, 2365-2392.

Campbell, K. W. (2007). Validation and update of hybrid empirical ground motion (attenuation) relations for the CEUS, NEHRP external research program, Final Technical Rept., U.S. Geol. Surv. Award No. 05HQGR0032.

Campbell, K. W., and Y. Bozorgnia (2003). Updated near-source ground motion (attenuation) relations for the horizontal and vertical components of peak ground acceleration and accel- eration response spectra, *Bull. Seism. Soc. Am.* **93**, 314–331.

Campbell, K. W., and Y. Bozorgnia (2006). Next generation attenuation (NGA) empirical ground motion models: can they be used in Europe?, in Proceedings, First European Conference on Earthquake Engineering and Seismology, Paper No. 458, Geneva, 10 pp.

Campbell, K. W., and Y. Bozorgnia (2008). NGA Ground Motion Model for the Geometric Mean Horizontal Component of PGA, PGV, PGD, and 5% Damped Linear Elastic Response Spectra for Periods Ranging from 0.01 to 10 s. *Earthquake Spectra* **24**, 139–171.

Chiu, J. M., A. C. Johnston, and Y. T. Yang, (1992). Imaging the Active Faults of the Central New Madrid Seismic Zone Using PANDA Array Data, *Seismol. Res. Lett.* **63**, 375-393.

Cox, R. T. and R. B. Van Arsdale (1997). Hotspot origin of the Mississippi embayment and its possible impact on contemporary seismicity. *Engineering Geology* **46**, 201-216.

Cox, R. T. and R. B. Van Arsdale (2002**)**. The Mississippi Embayment, North America: A first order continental structure generated by the Cretaceous superplume mantle event. *Jour. of Geodyn.* **34**, 63-176.

Cushing, E. M., E. H. Boswell and R. L. Hosman (1964). General Geology of the Mississippi Embayment. US Geological Survey Professional Paper 448-B, 28.

Dart, R. L. (1992). Catalog of pre-Cretaceous geologic drill-hole data from the upper Mississippi embayment: a revision and update of open-file report 90-260, *U.S. Geol. Surv. Open-File Rept. 92-685*.

EPRI (1988). Engineering model of earthquake ground motion for eastern North America, EPRI NP-6074, Electric Power Research Institute, Palo Alto, California.

Ervin, C. P., and L. D. McGinnis (1975). Reelfoot Rift-reactivated precursor to the Mississippi embayment, *Bull. Seism. Soc. Am.* **86**, 1,287- 1,295.

Fehler, M., and H. Sato (2003). Coda. *Pure and Applied Geophysics* **160**, 541–554.

Frankel, A., A. McGarr, J. Bicknell, J. Mori, L. Seeber and E. Cranswick (1990). Attenuation of high-frequency shear waves in the crust: measurements from New York state, South Africa, and southern California, *J. Geophys. Res.* **95,** 17,441-17,457.

Hamilton R. M. and F. A. McKeown (1988). Structure of the Blytheville arch in the New Madrid seismic zone. *Seismol. Res. Lett,* **59**, 117-21.

Hanks, T. and W. Thatcher (1972), A graphical representation of seismic source parameters. *J. Geophys. Res*. **77**, 4393-4405.

Harmsen, S. (1997). Estimating the diminution of shear-wave amplitude with distance: application to the Los Angeles, California, urban area, *Bull. Seism. Soc. Am*. **87**, 888-903.

Harrison, R. W. and A. Schultz (2002). Tectonic framework of the southwestern margin of the Illinois Basin and its influence on neotectonism and seismicity, *Seismol. Res. Lett.* **73**, 698-731.

Hildenbrand, T. G., M. F. Kane and J. D. Hendricks (1982). Magnetic basement in the upper Mississippi Embayment region-A preliminary report, *in* McKeown, F. A., and Pakiser, L., eds., Investigations of the New Madrid, Missouri, earthquake region: U.S. Geological Survey, Professional Paper 1236-E, p. 39-53.

Hosman, R. L. and J. S. Weiss (1991). Geohydrologic Units of the Mississippi Embayment and Texas Coastal Uplands Aquifer Systems, South-central United States. US Geological Survey Professional Paper 1416-B, 19 p.2.

Howe, J. R., and T. L. Thompson (1984). Tectonics, sedimentation, and hydrocarbon potential of the Reelfoot rift: *Oil and Gas Journal*. **82**, 179-190.

Idriss, I. M. (1985). “Evaluating Seismic Risk in Engineering Practice”, Theme Lecture No. 6, Proceedings, XI International Conference on Soil mechanics and foundation Engineering, San Fransisco, August, pp 265-320.

Idriss, I. M. (1987). “Earthquake Ground Motion”, lecture presented at EERI course on ‘Strong ground motion – seismic analysis, Design and Code Issues’, in Pasadena, California, on 10 April 1987.

Idriss, I. M. (1991). Selection of earthquake ground motions at rock sites, Report prepared for Structures Div., Building and Fire Research lab., NIST.

Johnson G. (2008). Earthquake Focal Mechanisms from the New Madrid Seismic Zone, *M.S. Thesis*, University of Memphis.

Johnston, A. C. (1996). Seismic moment assessment earthquakes in stable continental regions-III. New Madrid 1811-1812, Charleston 1886 and Lisbon 1755, *Geophys. J. Int.* **126**, 314-344.

Johnston, A. C. and E. S. Schweig (1996). The enigma of the New Madrid earthquakes of 1811-1812, *Annu. Rev. Earth Planet. Sci.* **24**, 339-384.

Kramer, S. (1996). Geotechnical earthquake engineering, Prentice Hall, Upper Saddle River, NJ, 07458, 653.

Langston, C. A., P. Boden, C. Powel, M. Withers, S. Horton, and W. Mooney (2005). Bulk sediment Q_P and Q_S in the Mississippi Embayment, central United States, *Bull. Seismol. Soc. Am.* **95,** 2162-2179.

Malagnini, L., A. Akinci, R. B. Herrmann, N. A. Pino, and L. Scognamiglio (2002). Characteristics of the ground motion in Friuli (northeastern Italy), *Bull. Seism. Soc. Am.* **92**, 2186–2204.

Malagnini, L., R. B. Herrmann, and M. Di Bona (2000). Ground motion scaling in the Apennines (Italy), *Bull. Seism. Soc. Am.* **90,** 1062–1081.

Miao, Q. and C. A. Langston (2007). Empirical distance attenuation and the local magnitude scale for the central U.S. *Bull. Seism. Soc. Am.* **97**,2,137 –2,151.

Mitchell, B. J., O. W. Nuttli, R. B. Herrmann and W. Stauder (1991). Seismotectonics of the central United States, in *Neotectonics of North America*, D. B. Slemmons, E. R. Engdahl, M. D. Zoback and D. D. Blackwell, eds., Geological Society of America, Boulder, pp 245-260.

Murray, G. E. (1961). Geology of the Atlantic and Gulf Coastal Province of North America. Harper and Brothers, New York, NY.

Narayan, J. P. (2001). Site specific ground motion prediction using 3-D modelling, ISET *J. Earthq. Techn.* **38**, 17–29.

Nuttli, O. W. (1973). The Mississippi valley earthquakes of 1811 and 1812: intensities, ground motion and magnitude, *Bull. Seism. Soc. Am.* **63**, 227-248.

Parrish, S., and R. Van Arsdale (2004). Faulting along the southeastern margin of the Reelfoot rift in northwestern Tennessee revealed in deep seismic reflection profiles, *Seismol. Res. Lett.* **75**, 782-791.

Petersen, M. D., A. D. Frankel, S. C. Harmsen, C. S. Mueller, K. M. Haller, R. L. Wheeler, R. L. Wesson, Y. Zeng, O. S. Boyd, D. M. Perkins, N. Luco, E. H. Field, C. J. Wills, and K. S. Rukstales (2008). Documentation for the 2008 update of the United States national seismic hazard maps, U.S. Geol. Surv. Open-File Rept. 2008-1128.

Pujol, J., S. Pezeshk, Y. Zhang, and C. Zhao (2002). Unexpected values of Q_S in the unconsolidated sediments of the Mississippi Embayment, *Bull. Seismol. Soc. Am.* **92,** 1117-1128.

Raoof, M., R. B. Herrmann, and L. Malagnini (1999). Attenuation and excitation of three-component ground motion in Southern California, *Bull. Seism. Soc. Am.* **89**, 888–902.

Rautian, T. G. and V. I. Khalturin (1978). The use of the coda for determi- nation of the earthquake source spectrum, *Bull. Seism. Soc. Am.* **68**, 923-948.

Samiezade´-Yazd, M., R. B. Herrmann, L. Malagnini, and W. Liu (1996). A regional comparison of vertical ground motion in North America. Report 1434-94-G-2403.

Stearns, R. (1957). Cretaceous, Paleocene, and lower Eocene geologic history of the northern Mississippi embayment, *Bull. Geol. Soc. Am.* **68,** 1077–1100.

Thomas, W. A. (1985). The Appalachian-Ouachita connection: Paleozoic orogenic belt at the southern margin of North America: *Annual Review of Earth and Planetary Sciences* **13**, 175-199.

Thomas, W. A. (1991). The Appalachian-Ouachita rifted margin of southeastern North America, *Bull. Geol. Soc. Am.* **103**, 415–431.

Thomas, W. A. (2006). Tectonic inheritance at a continental margin. *GSA Today* **16**.

Toro, G. R. and R. K. McGuire (1987). An investigation into earthquake ground motion characteristics in eastern North America, *Bull. Seism. Soc. Am.* **77**, 468-489.

Tsumura, K. (1967). Determination of earthquake magnitude from duration of oscillation, *Zisin* (in Japanese), 30-40.

Tuttle, M. P., E. S. Schweig, J. D. Sims, R. H. Lafferty, L. W. Wolf, and M. L. Haynes (2002). The earthquake potential of the New Madrid seismic zone, *Bull. Seism. Soc. Am.* **92**, 2080-2089.

Wang, Z., R. Street, E. Woolery, and J. Harris (1994). Q_S estimation for unconsolidated sediments using first-arrival *SH* wave critical refractions, *J. Geophys. Res.* **99,** 13543-13551.

Zoback M. L. and M. D. Zoback (1980). State of stress in conterminous United States, *J. Geophys. Res.* **85**, 6113-6156.

Appendix A

Supplementary figures for estimating the distance term D

The figure in section 3.3 is an example of the overall work done for all the frequencies. This initial estimate of the distance term is performed in stages as indicated before, with first being the binning of the normalized amplitude at different distances in order to find a mean amplitude representative at that distance. Then second step in the process, being the interpolation of the binned amplitudes with distance, to provide a sketch of the attenuation function, and therefore the first estimate of the hinges of the geometrical spreading. Then lastly a multi-linear fit of the interpolation to find the best-fit equation. This three –step process is applied to each frequency separately then the resultant combined together for forward modeling. Figure A-1 to A-11 is an illustration of the process of initial estimate of D for a normalized time series filtered at different ferquencies. Top left panel illustrates the coda-normalized peak velocity distribution estimated using the coda normalization technique. The line interpolates (interpolation) the mean points binned within a distance window. The top right panel illustrates a bilinear cubic least-square fit (CLS fit) of the interpolation, while bottom left shows a forward model (EQ fit) of the least-square fit for the attenuation function (i.e. the distance term). The bottom right panel illustrates the residual of the regression analysis.

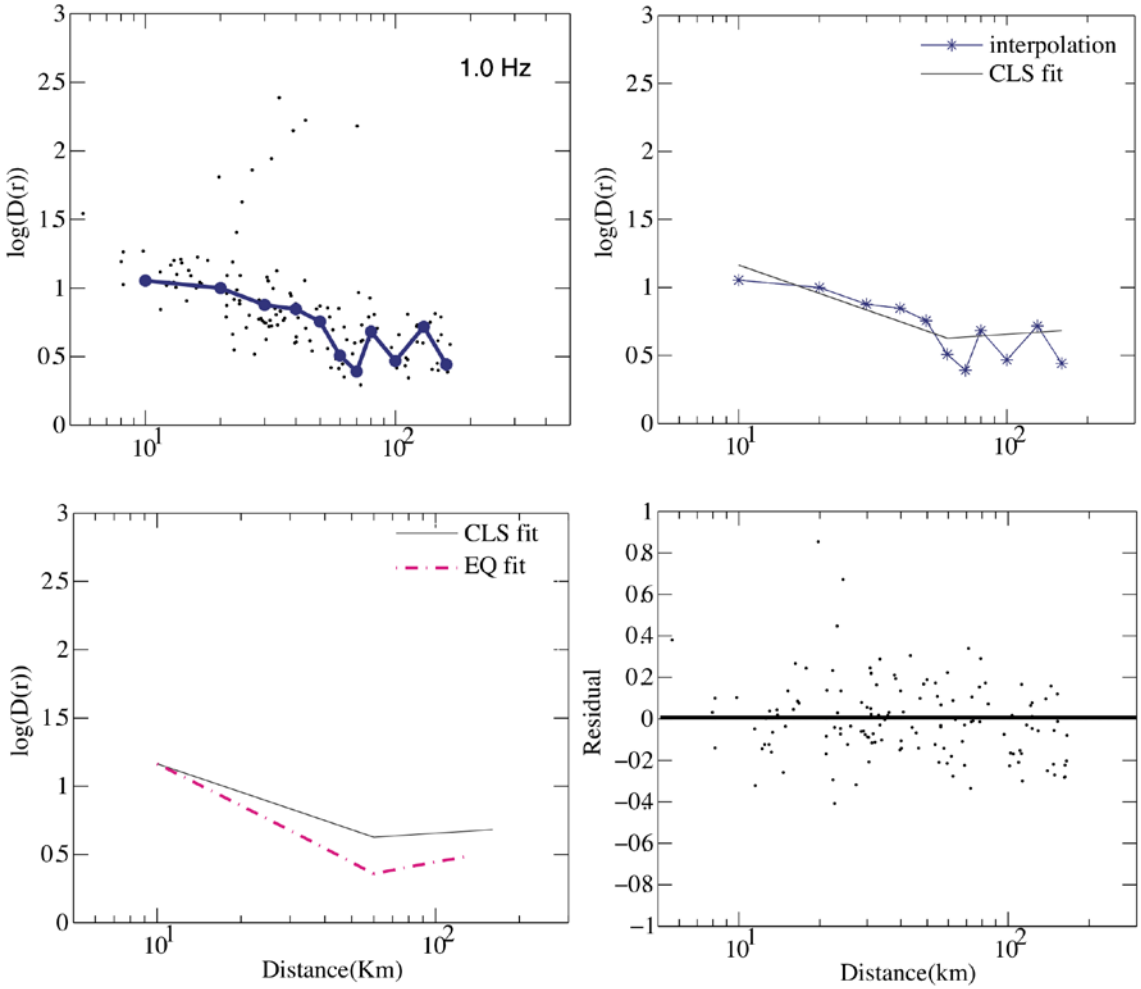

Figure A 1: Regression of coda-normalized peak velocities at 1.0 Hz obtained for NMSZ local events. The gray dots indicate individual normalized peak estimates, the rounded (asterisks) are mean peak estimates of the individual peaks binned at the respective distances, and lines denote the different fitting lines of the binned duration estimates.

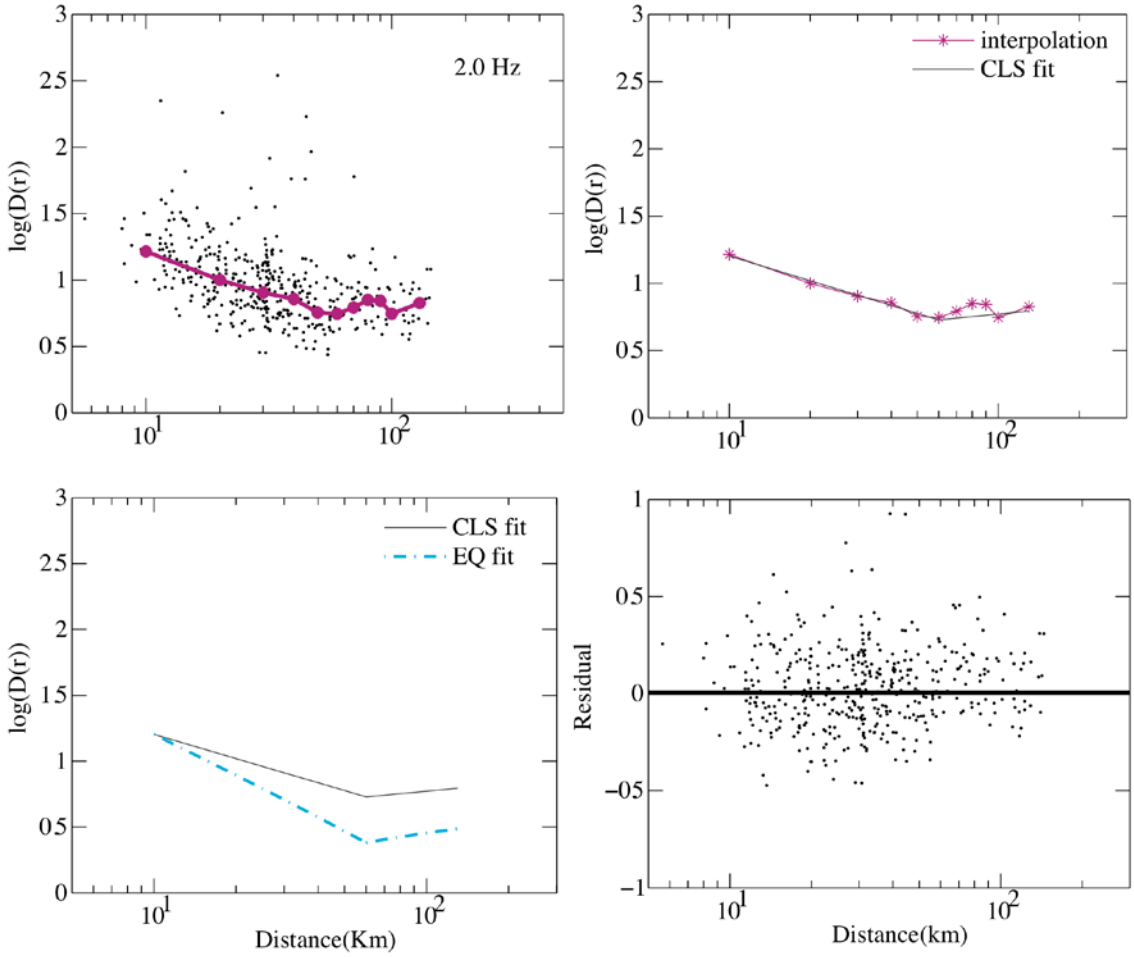

Figure A 2: Regression of coda-normalized peak velocities at 2.0 Hz obtained for NMSZ local events. The gray dots indicate individual normalized peak estimates, the asterisks are mean peak estimates of the individual peaks binned at the respective distances, and lines denote the different fitting lines of the binned duration estimates.

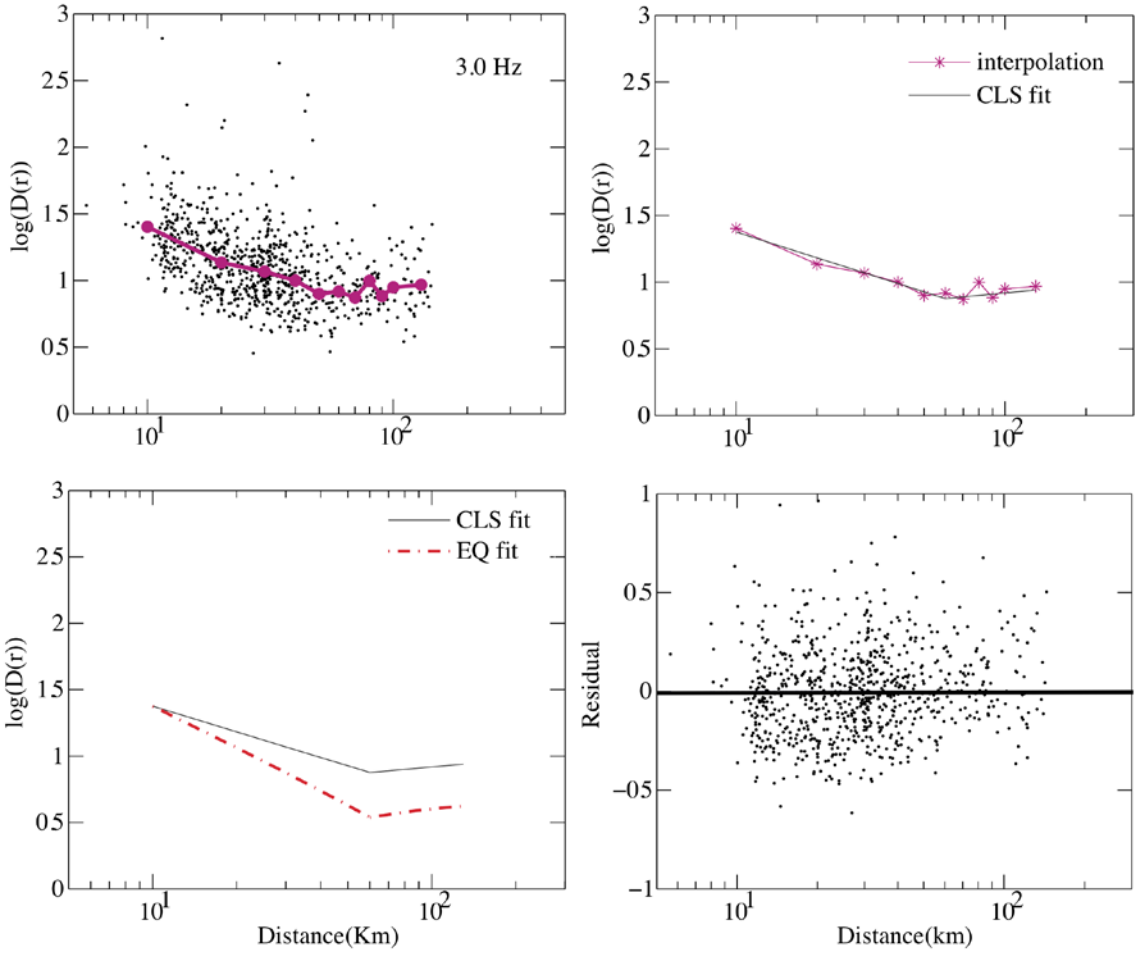

Figure A 3: Regression of coda-normalized peak velocities at 3.0 Hz obtained for NMSZ local events. The gray dots indicate individual normalized peak estimates, the asterisks are mean peak estimates of the individual peaks binned at the respective distances, and lines denote the different fitting lines of the binned duration estimates.

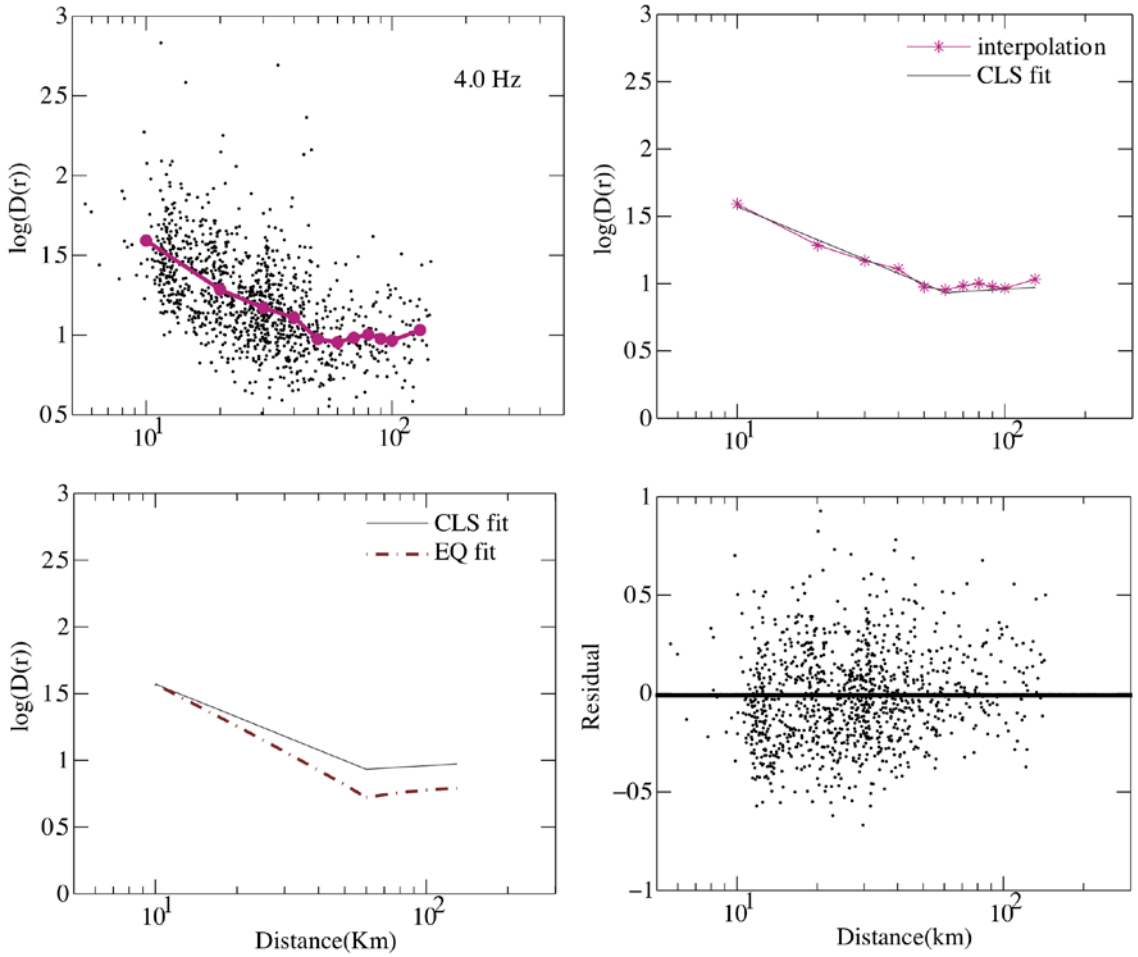

Figure A 4: Regression of coda-normalized peak velocities at 4.0 Hz obtained for NMSZ local events. The gray dots indicate individual normalized peak estimates, the asterisks are mean peak estimates of the individual peaks binned at the respective distances, and lines denote the different fitting lines of the binned duration estimates.

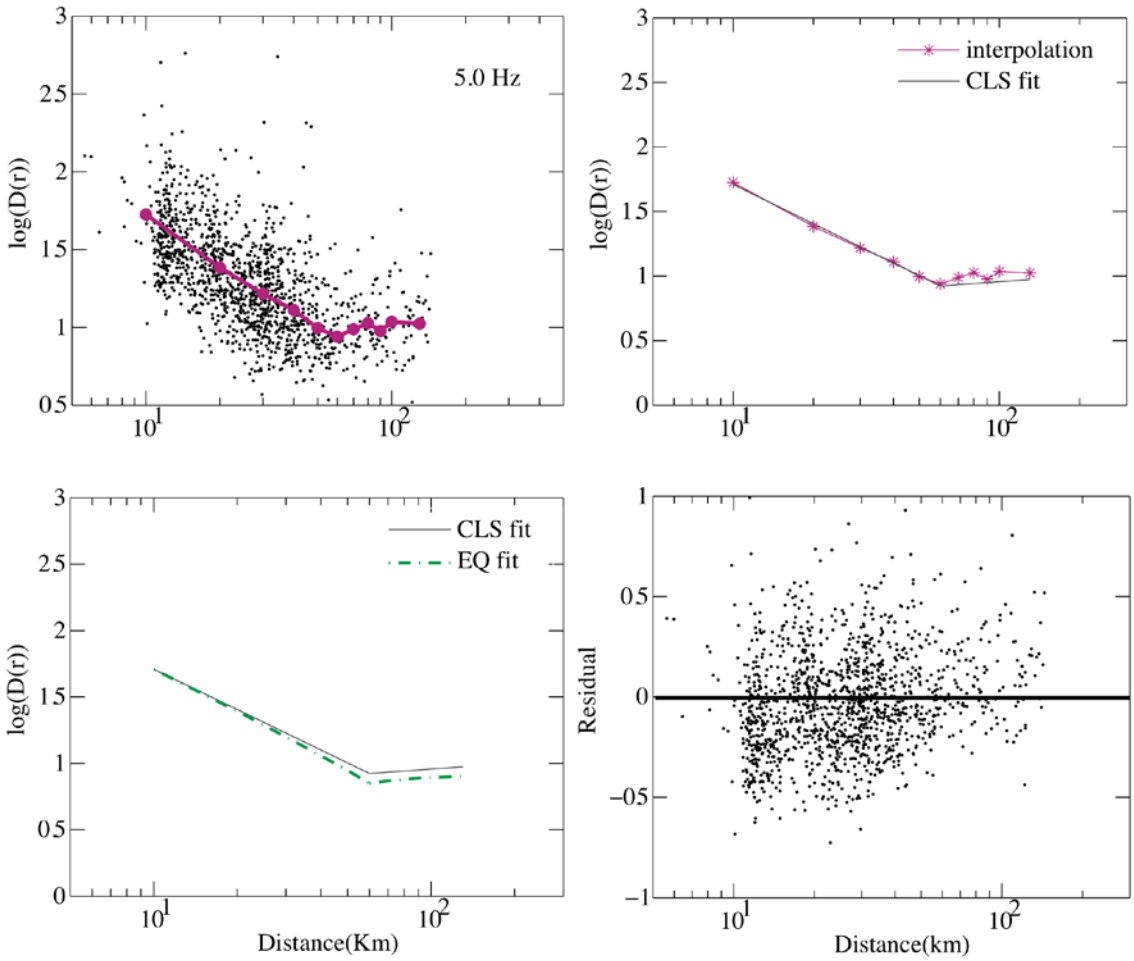

Figure A 5: Regression of coda-normalized peak velocities at 5.0 Hz obtained for NMSZ local events. The gray dots indicate individual normalized peak estimates, the asterisks are mean peak estimates of the individual peaks binned at the respective distances, and lines denote the different fitting lines of the binned duration estimates.

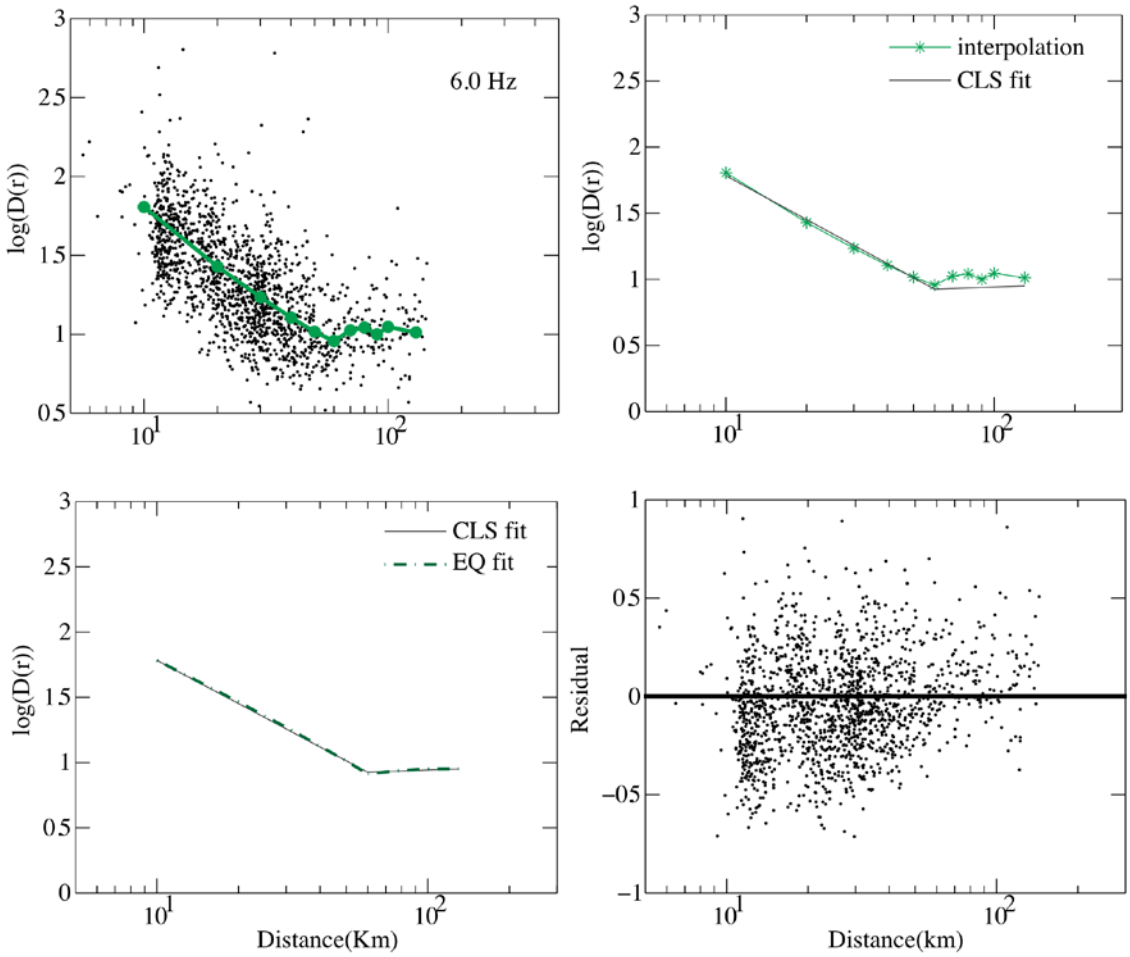

Figure A 6: Regression of coda-normalized peak velocities at 6.0 Hz obtained for NMSZ local events. The gray dots indicate individual normalized peak estimates, the asterisks are mean peak estimates of the individual peaks binned at the respective distances, and lines denote the different fitting lines of the binned duration estimates.

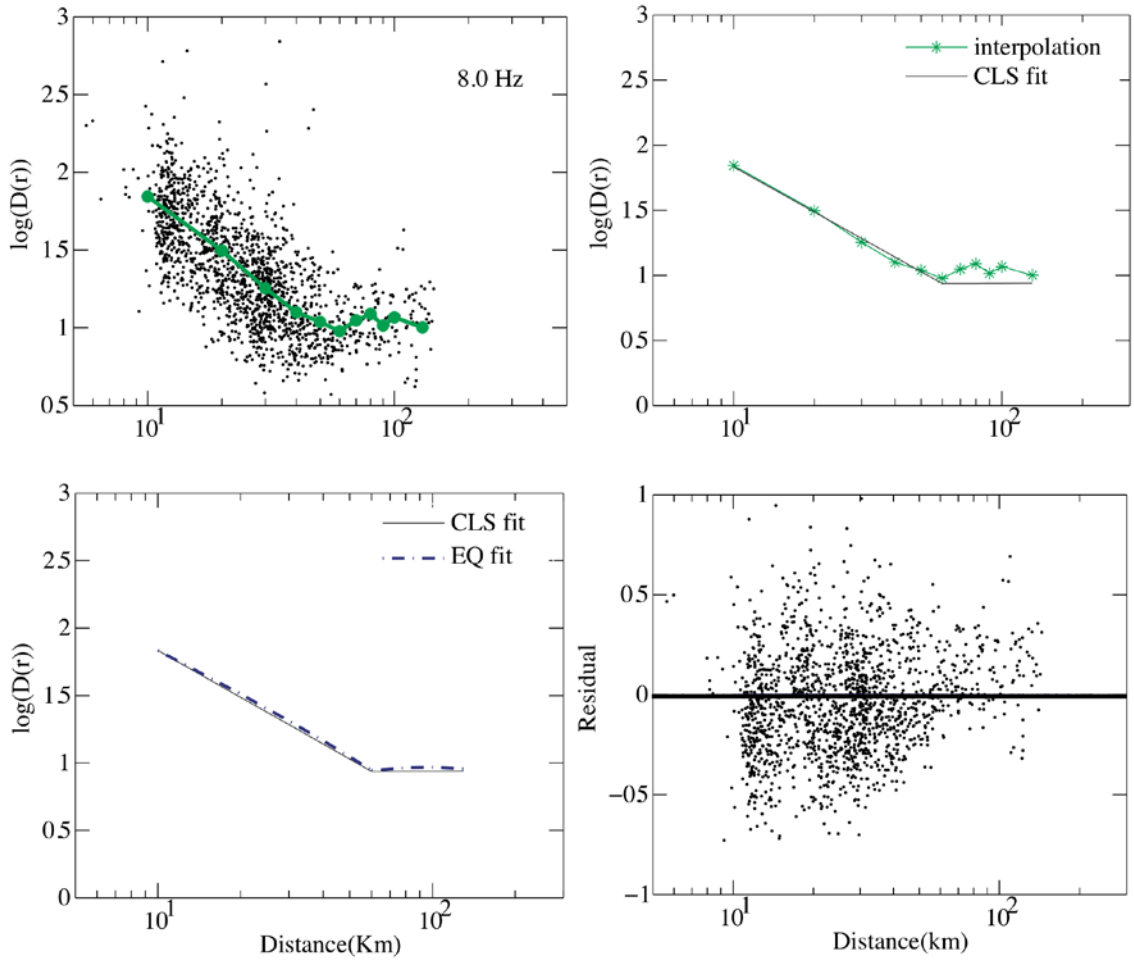

Figure A 7: Regression of coda-normalized peak velocities at 8.0 Hz obtained for NMSZ local events. The gray dots indicate individual normalized peak estimates, the asterisks are mean peak estimates of the individual peaks binned at the respective distances, and lines denote the different fitting lines of the binned duration estimates.

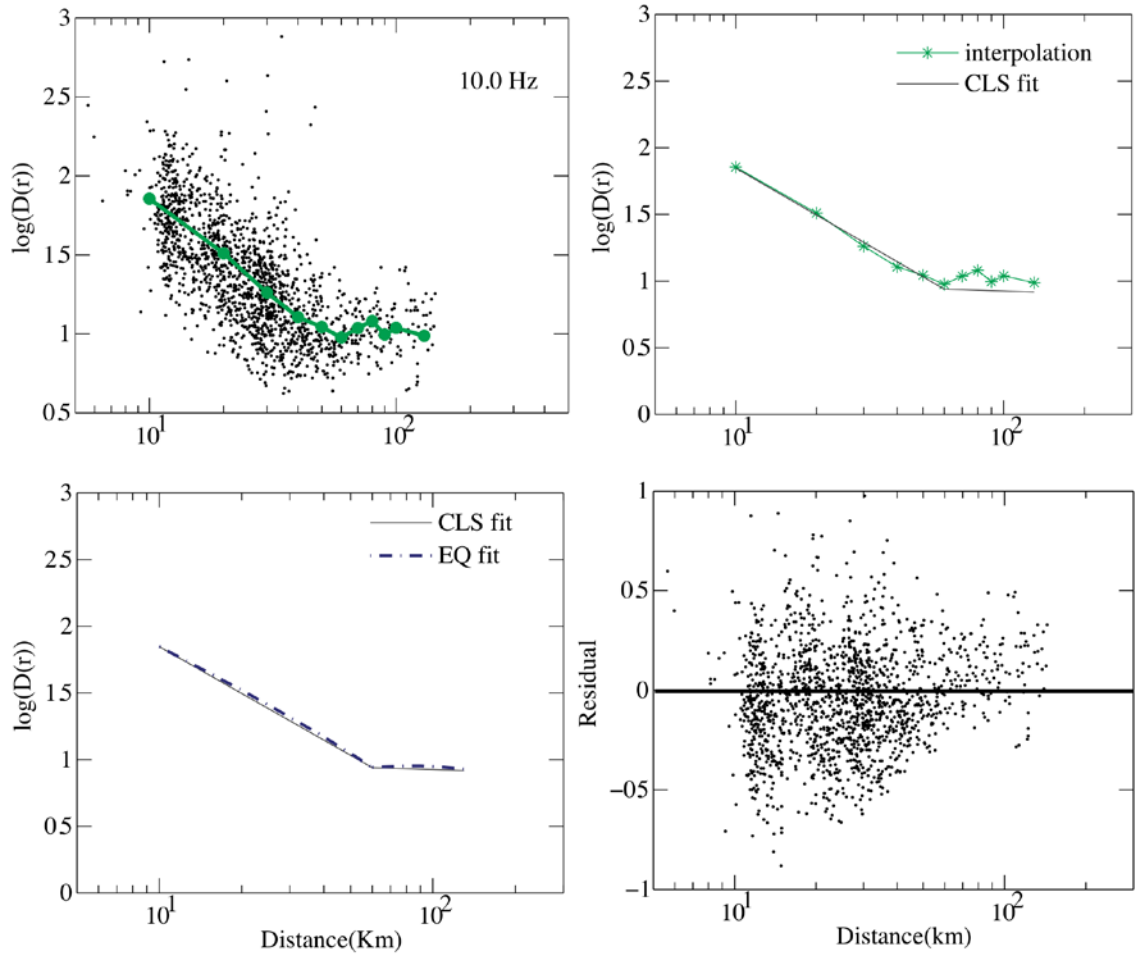

Figure A 8: Regression of coda-normalized peak velocities at 10.0 Hz obtained for NMSZ local events. The gray dots indicate individual normalized peak estimates, the asterisks are mean peak estimates of the individual peaks binned at the respective distances, and lines denote the different fitting lines of the binned duration estimates.

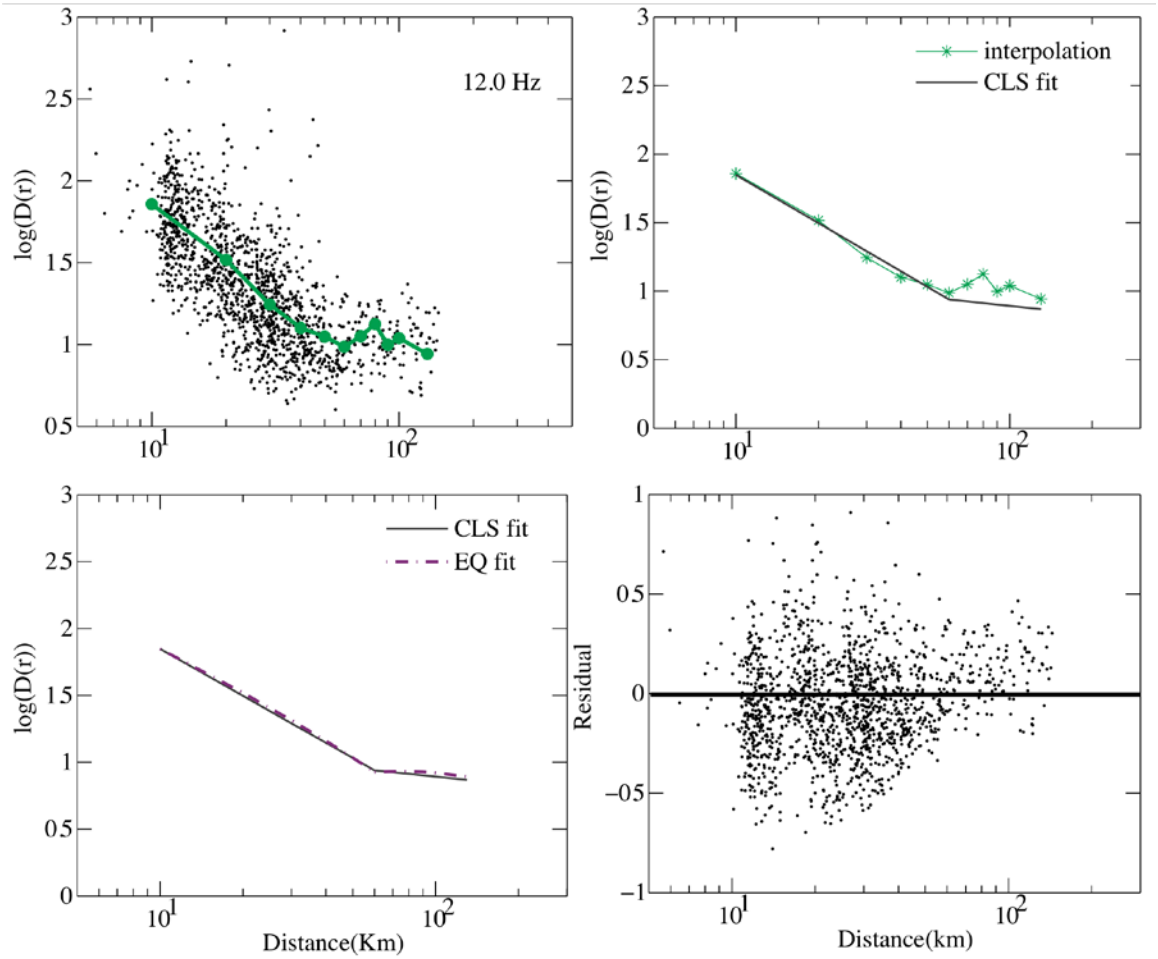

Figure A 9: Regression of coda-normalized peak velocities at 12.0 Hz obtained for NMSZ local events. The gray dots indicate individual normalized peak estimates, the grey asterisks are mean peak estimates of the individual peaks binned at the respective distances, and lines denote the different fitting lines of the binned duration estimates.

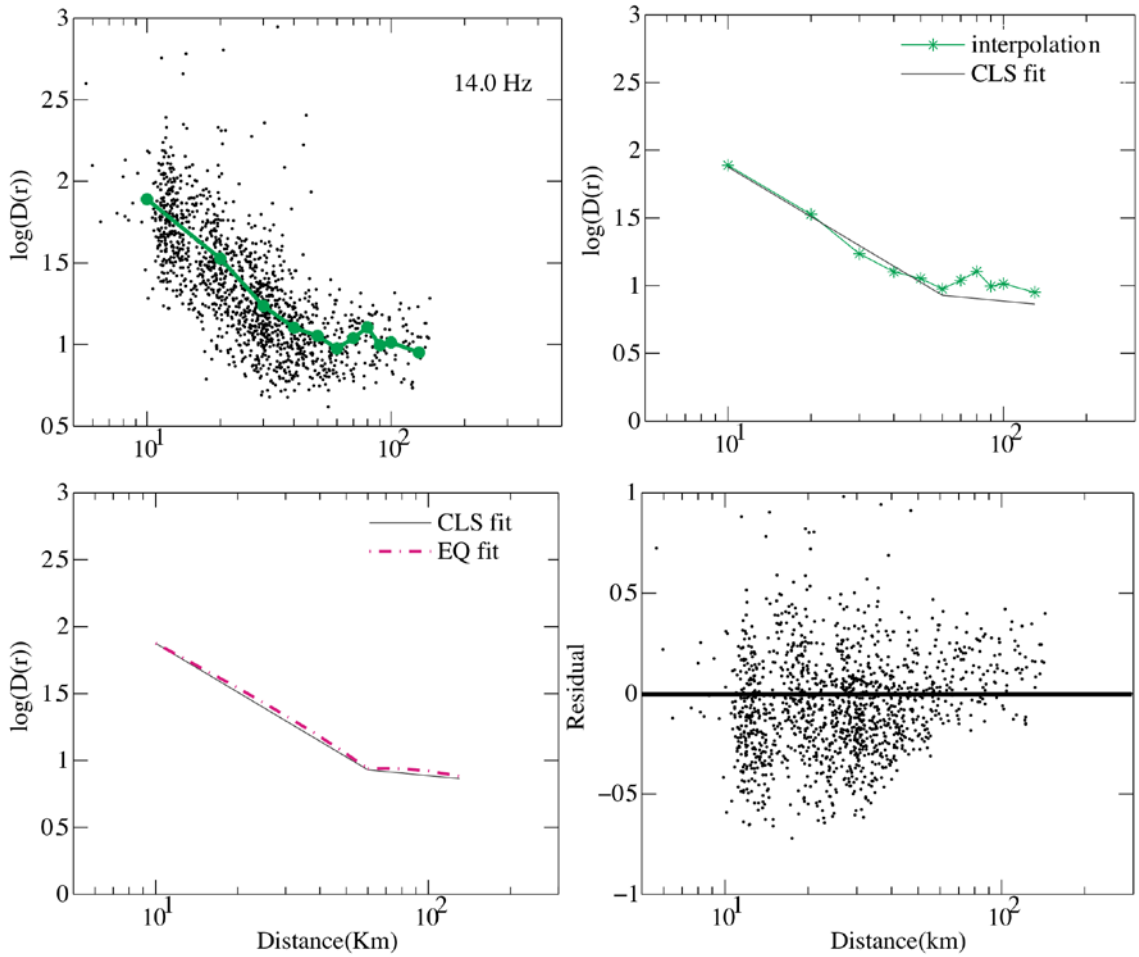

Figure A 10: Regression of coda-normalized peak velocities at 14.0 Hz obtained for NMSZ local events. The gray dots indicate individual normalized peak estimates, the asterisks are mean peak estimates of the individual peaks binned at the respective distances, and lines denote the different fitting lines of the binned duration estimates.

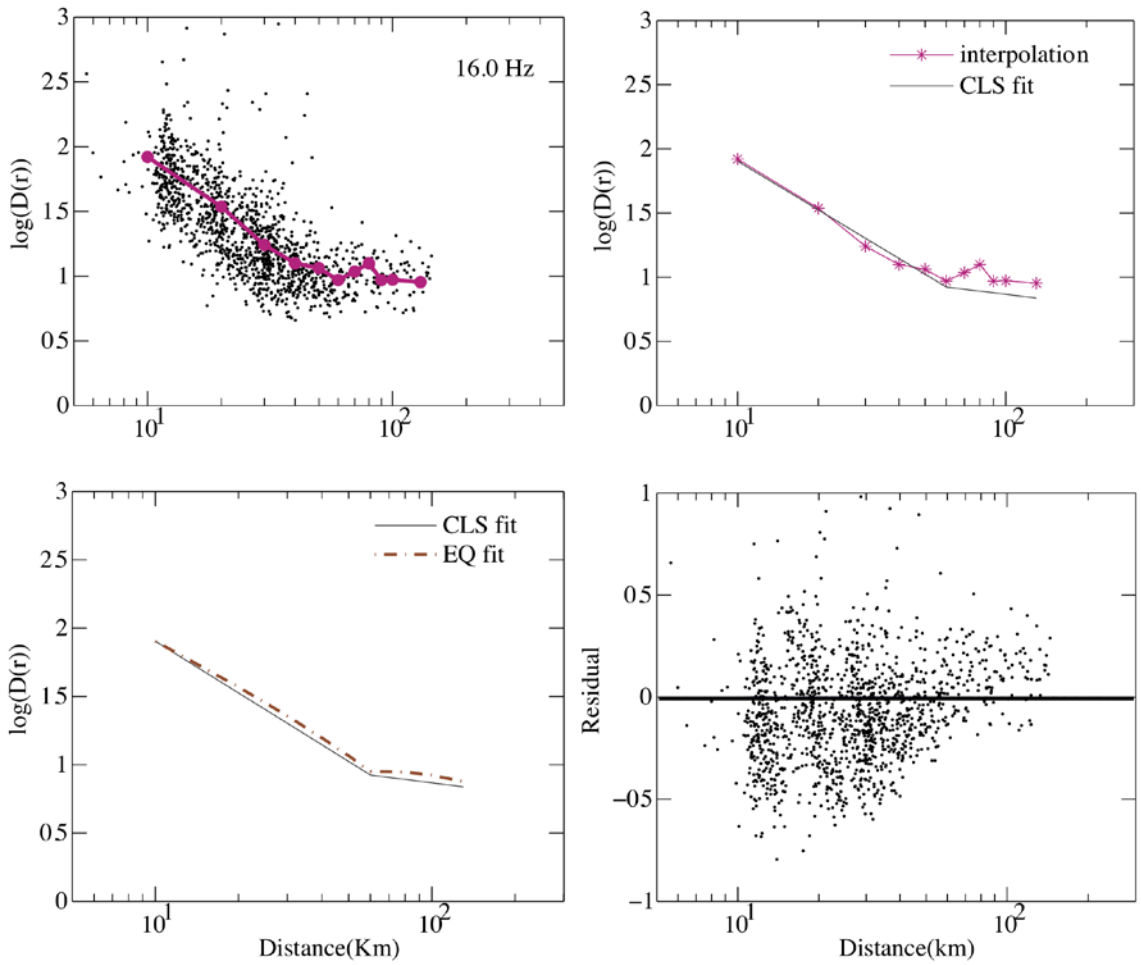

Figure A 11: Regression of coda-normalized peak velocities at 16.0 Hz obtained for NMSZ local events. The gray dots indicate individual normalized peak estimates, the grey asterisks are mean peak estimates of the individual peaks binned at the respective distances, and lines denote the different fitting lines of the binned duration estimates.

Appendix B

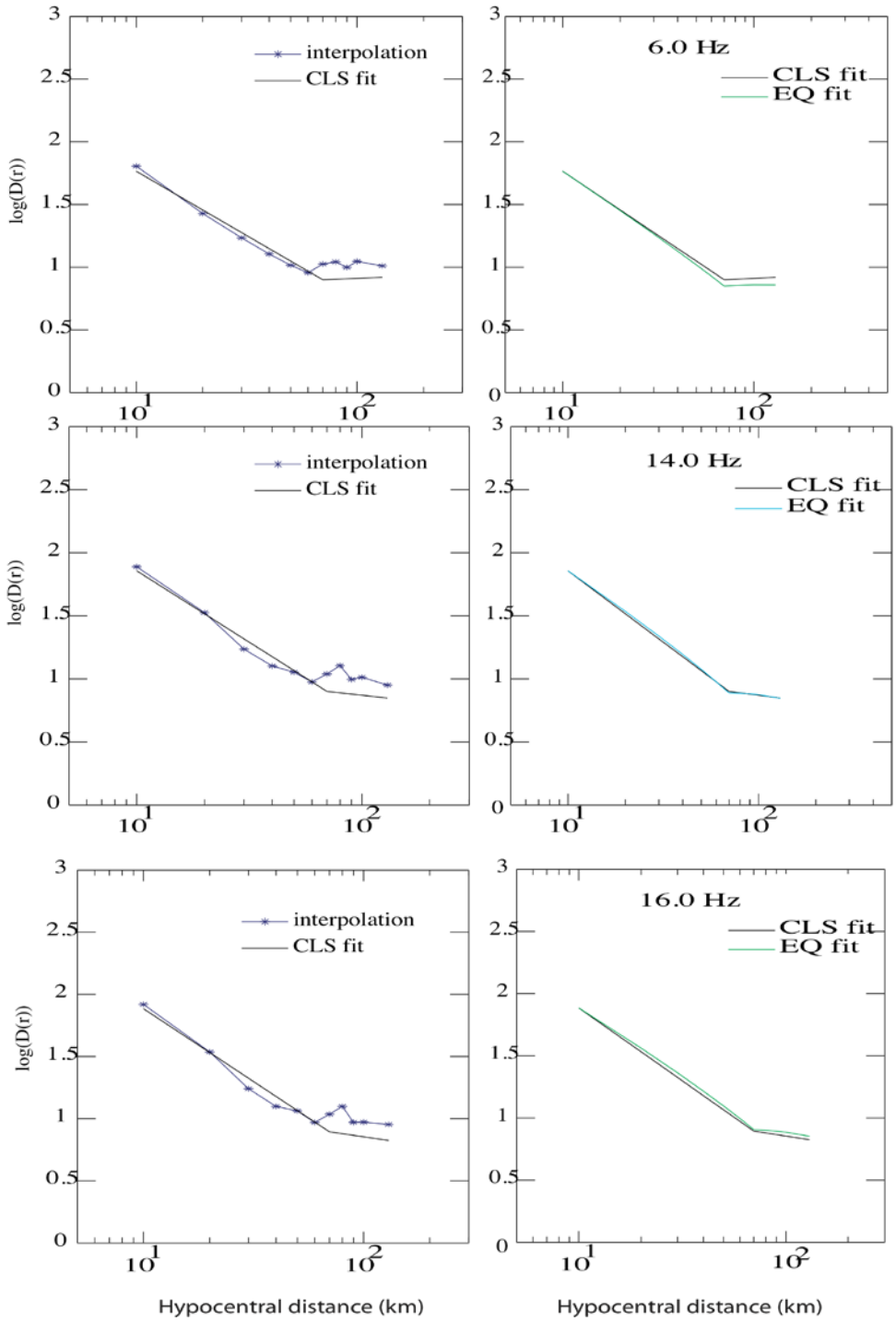

Figure B 1: Regression of coda-normalized peak velocities at 6,14 and16.0 Hz at $r = 70km$ fitting r^{-1},$1050 f^{0.35}$. The grey asterisks are mean peak estimates of the individual peaks binned at the respective distances, and lines denote the different fitting lines of the binned duration estimates.

Appendix C

Dataset used to estimate seismic moment.

Table C- 1: Source parameters for strike slip events (M_D<3) used for plotting figures 3-10 and 3-11.

Event Date	M_D	Seismic moment (Nm)	M_W	Depth (km)	Corner frequency (Hz)	Stress drop (bar)
20001006	2.2	5.01E+12	2.43	7.9	7	3.2
20001104	2.4	7.08E+12	2.53	7.56	7	4.5
20010613	2.4	5.99E+13	3.15	10.26	5	13.9
20020728	1.7	1.76E+12	2.13	5.7	7	1.1
20030707	2.6	1.50E+13	2.75	8.92	7	9.6
20030805	2.6	1.00E+13	2.63	14.68	10	18.6
20030829	2.2	5.79E+12	2.48	11.8	6	2.3
20040209	1.8	1.76E+12	2.13	9.02	9	2.4
20040217	1.9	1.76E+12	2.13	5.28	7.5	1.4
20040312	1.8	1.76E+12	2.13	7.7	8	1.7
20041215	2.4	5.09E+12	2.44	19.02	10	7.7
20050104	1.7	1.09E+12	1.99	11	10	2.0
20050111	2.1	6.79E+12	2.52	7	9	9.2
20050127	1.8	2.80E+12	2.26	9.33	8	2.7
20050303	1.9	2.90E+12	2.27	8.29	6	1.2
20050309	1.8	2.90E+12	2.27	7.59	9	3.9
20050419	1.8	1.78E+12	2.13	8.1	8	1.7
20050428	2.5	1.77E+13	2.80	8.8	12	56.9
20050430	1.8	2.70E+12	2.25	8.33	11	6.7
20050501	2.2	7.08E+12	2.53	10	5	1.6
20050510	2.2	7.07E+12	2.53	9.4	5.5	2.2
20050608	1.7	1.26E+12	2.03	4.76	6	0.5
20050702	1.8	1.26E+12	2.03	7.17	9	1.7
20050713	2.8	4.00E+13	3.03	10.76	6	16.1
20050718	2.3	1.30E+13	2.71	9.08	5.5	4.0
20050814	1.6	2.25E+12	2.20	6.6	9	3.1
20050817	2	4.26E+12	2.39	11.74	7	2.7
20051225	1.6	1.58E+12	2.10	9.2	7	1.0
20051225	2.8	3.98E+13	3.03	12.3	9	54.0
20060202	1.6	1.26E+12	2.03	6.09	9	1.7
20060303	1.9	2.02E+12	2.17	8	9	2.7
20060324	1.8	1.30E+12	2.04	6.5	10	2.4
20060412	1.7	1.30E+12	2.04	8.5	12	4.2
20060412	1.8	1.30E+12	2.04	7	10	2.4
20060511	2.1	1.24E+13	2.70	10	9	16.8
20060605	1.9	3.50E+12	2.33	9.8	10	6.5
20060617	1.7	5.60E+11	1.80	7.9	10	1.0

20060702	2.4	8.59E+12	2.59	12	8	8.2
20060727	2.2	7.90E+12	2.57	12	8	7.5
20060813	2.2	6.60E+12	2.51	8	8	6.3
20060922	2	3.59E+13	3.00	8.8	9	48.7
20060925	1.9	1.26E+12	2.03	7.9	8	1.2
20061020	2	2.20E+13	2.86	8.4	10	41.0
20061020	1.7	1.00E+13	2.63	7.9	7	6.4
20061020	1.9	1.00E+13	2.63	8.9	10	18.6
20061023	1.9	2.52E+12	2.23	6.3	10	4.7
20061130	2.1	2.00E+13	2.83	11.2	8	19.1
20070121	2.4	2.00E+13	2.83	7.47	5	4.7
20070203	2	8.30E+12	2.58	8.2	7	5.3
20070403	2.3	2.25E+13	2.87	7.6	12	72.5
20070406	2.7	6.41E+13	3.17	10.62	6	25.8
20070515	2.4	2.84E+13	2.94	7.8	5	6.6
20070625	2	1.24E+13	2.70	7.7	9	16.8
20070628	1.8	6.20E+12	2.49	8.16	9	8.4
20070708	2.3	3.55E+13	3.00	2.3	8	47.0
20070815	1.8	5.08E+12	2.44	14.9	10	9.5
20070903	2.6	1.55E+13	2.76	4.7	7	13.7

Table C- 2: Source parameters for reverse fault events (M_D<3) used for plotting figures 3-10 and 3-11.

Event Date	M_D	Seismic moment (Nm)	M_W	Depth (km)	Corner frequency (Hz)	Stress drop (bar)
20001232	2	5.60E+12	2.47	13.9	7	3.6
20010731	2.5	2.07E+13	2.84	8.53	9	28.1
20010913	1.7	8.90E+11	1.93	8.99	7.5	0.7
20010927	1.8	2.51E+12	2.23	10.48	8	2.4
20011111	1	2.51E+12	2.23	9.03	9	3.4
20011216	2.1	7.50E+12	2.55	4.95	5.5	2.3
20020805	1.7	2.51E+12	2.23	8.82	7.5	2.0
20030109	2	2.51E+12	2.23	7.7	9	3.4
20030209	2.3	6.50E+12	2.51	12.84	5	1.5
20030530	2.8	7.50E+12	2.55	6.16	9	10.2
20030730	2.8	8.50E+12	2.59	5.39	11	21.1
20030805	1.6	8.50E+11	1.92	8.25	9	1.2
20040109	1.8	8.50E+11	1.92	8.38	10	1.6
20040201	2.3	3.50E+12	2.33	8.72	9	4.7
20040515	2.2	2.51E+13	2.90	12.24	7	16.0
20050324	1.7	2.51E+12	2.23	6.23	9	3.4
20050502	2.4	1.00E+13	2.63	9.9	5.5	3.1
20050710	2	3.12E+12	2.30	13.81	8	3.0

20050718	2	2.28E+12	2.21	8.33	8	2.2
20051001	1.6	1.08E+12	1.99	4.85	10	2.0
20051019	2.5	2.51E+12	2.23	8.07	9	3.4
20051117	2	2.51E+12	2.23	9.91	10	4.7
20051210	1.7	2.51E+12	2.23	7.1	10	4.7
20051214	1.9	2.51E+12	2.23	15.49	10	4.7
20060109	1.8	2.51E+12	2.23	8.59	10	4.7
20060118	2	1.51E+12	2.09	6.58	7	1.0
20060206	1.8	1.05E+12	1.98	17.32	8.5	1.0
20060207	1.6	3.52E+11	1.66	7.42	9	0.5
20060210	2.1	2.51E+12	2.23	3.46	9	4.7
20060308	2.6	1.08E+13	2.66	10.65	9	14.6
20060308	1.8	8.90E+11	1.93	10.44	8	0.8
20060312	1.8	2.51E+12	2.23	6.05	8	2.4
20060523	1.6	7.56E+11	1.89	6.34	8	0.7
20060523	2.5	9.56E+12	2.62	8.57	9	13.0
20060705	1.8	7.51E+11	1.88	6.52	9	1.0
20060730	1.7	7.51E+11	1.88	6.46	5	0.2
20060730	1.8	2.06E+12	2.18	8.53	8	2.0
20060730	2.3	8.50E+12	2.59	5.38	7	5.4
20060804	1.6	8.16E+11	1.91	10.19	9	1.1
20060828	2	8.16E+12	2.57	9.16	9	11.1
20060915	1.8	5.16E+12	2.44	10.45	10	9.6
20061021	1.6	4.16E+12	2.38	7.3	9	5.6
20061202	1.6	4.16E+12	2.38	7.5	10	7.7
20061215	2.3	1.55E+13	2.76	12.35	10	28.8
20061217	2.3	1.55E+13	2.76	6.3	9	21.0
20061227	1.6	7.60E+12	2.55	8.36	7	4.9
20070106	1.7	3.23E+12	2.31	7.47	10	6.0
20070113	1.8	1.23E+13	2.69	8.77	12	39.6
20070221	2	1.26E+13	2.70	7.58	9	17.1
20070302	1.8	7.60E+12	2.55	6.48	5	1.8
20070308	1.6	3.60E+12	2.34	8.78	10	6.7
20070314	2	1.62E+13	2.77	9.08	7	10.4
20070314	1.7	6.47E+12	2.51	8.19	9	8.8
20070428	2	6.47E+12	2.51	7.72	10	12.0
20070429	1.7	3.62E+12	2.34	6.26	12	11.6
20070520	2.2	6.47E+12	2.51	5.25	10	12.0
20070531	2.2	2.25E+13	2.87	4.77	9	30.5
20070612	1.6	2.25E+12	2.20	7.4	10	4.2
20070709	2.4	2.25E+13	2.87	7.54	8	21.4
20071001	2.3	2.25E+13	2.87	6.6	10	41.8
20071016	1.8	4.22E+12	2.38	8.98	10	7.9
20071018	2.3	4.22E+13	3.05	6.5	10	78.6
20071122	2.5	4.22E+13	3.05	6.72	10	78.6

Table C- 3: Source parameters for M_W>3 events used for plotting figures 3-10 and 3-11.

Event Date	M_W	Seismic moment (Nm)	Depth (km)	Corner frequency (Hz)	Stress drop (bar)
20010707	3.1	5.60E+13	13.87	4	6.7
20030502	3.2	7.94E+13	0.09	8	75.7
20030430	4	8.91E+14	23.68	4	106.2
20040615	3.5	2.24E+14	4.54	4	26.7
20040716	3.5	2.24E+14	4.41	7	142.9
20050210	4.1	7.09E+14	15.48	5	165.0
20050501	4.2	1.25E+15	10	4	148.9
20050602	4	8.90E+14	15.02	4.5	151.0
20050620	3.6	4.46E+14	18.72	5	103.8
20060907	3.3	1.58E+14	7.56	5	36.8
20060606	4	1.26E+15	2.5	4	150.0